

1 **Characterizing geologic and climatic controls on rockfall hazards** 2 **using an inventory and integrated kinematic and runout model:** 3 **Skagway, Alaska, USA**

4 Ian D. Wachino¹, Joshua J. Roering¹, Reuben Cash², and Annette I. Patton^{3,4}

5 ¹Department of Earth Sciences, University of Oregon, Eugene, OR, 97403, USA

6 ²Environmental Department, Skagway Traditional Council, Skagway, AK, 99840, USA

7 ³Sitka Sound Science Center, Sitka, AK, 99835, USA

8 ⁴College of Forestry, Oregon State University, Corvallis, OR, 97331, USA

9 *Corresponding author:* Joshua J. Roering (jroering@uoregon.edu)

10 **Abstract**

11 Rockfall is common in steep terrain and poses a hazard to nearby communities. While rockfall triggering mechanisms are
12 highly variable and difficult to quantify, the susceptibility of rock slopes to planar, wedge, or toppling failure can be readily
13 assessed using kinematic analysis. As such, valley slopes with favourable joint orientations exhibit high rockfall
14 susceptibility although the potential for rockfall runout to impact infrastructure and public safety depends on the morphology
15 of downslope terrain. Integrating rockfall susceptibility and runout models with maps of talus deposits accumulated from
16 past rockfall events is an effective combination of tools to inform mitigation but can be difficult to accomplish across
17 extensive areas. Here, we combine these methods with a rockfall inventory spanning 2005 to 2022 to assess geologic and
18 climate controls on rockfall activity in the steep and forested postglacial valleys proximal to Skagway, Alaska, where recent
19 rockfall activity has imperilled public safety, infrastructure, and tourism. The inventory reveals rockfall activity throughout
20 the year with peak activity in early spring that coincides with a rapid rise in minimum daily temperatures. Our field
21 investigations identified two steeply dipping orthogonal joint sets that favour toppling failure along NW-facing hillslopes in
22 the lower Skagway River valley as well as the NW-facing valleys that bound nearby Dyea Bay and Nahku Bay. We used
23 new and existing lidar data and 405 field-derived joint orientations to inform a kinematic toppling failure model that
24 identifies source zones upslope of abundant talus slopes that we mapped from field observations and lidar analyses. We
25 coupled the source zones with RAMMS:Rockfall to simulate 197,800 rockfall runout events for scenarios with varying block
26 size and ground cover. The runout predictions highlight zones of low and high rockfall propagation susceptibility that is
27 negatively correlated with hillslope roughness which results from the combined influence of joint orientations that generate
28 bedrock benches and the spatial pattern of glacial erosion. High-hazard segments of the ridgeline exhibit distinct bedrock
29 cliffs and slope-spanning talus slopes that result from the accumulation of rockfall activity over millennia. Taken together,
30 our findings illustrate past controls on rockfall location and timing to inform mitigative measures.

31 **1 Introduction**

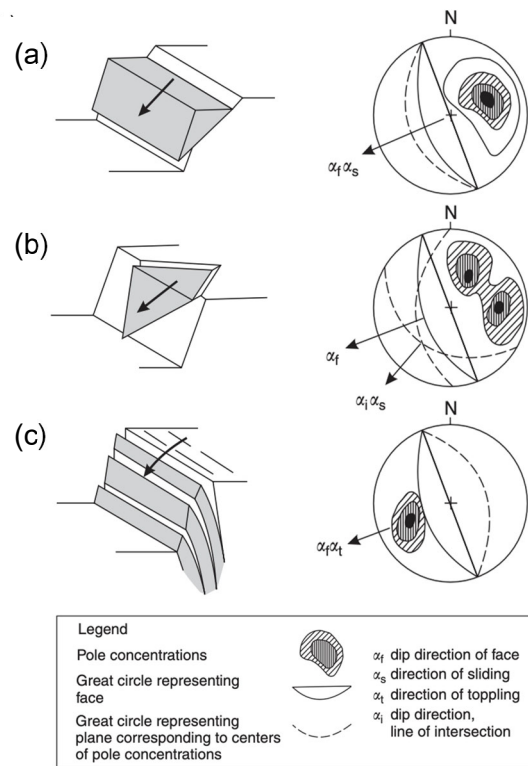
32 In steep, rocky landscapes, the detachment and downslope movement of discrete rock fragments (i.e., rockfall) can occur
33 frequently and poses a significant hazard to proximal communities and infrastructure (Hungre et al., 2014). Rockfall activity
34 has been attributed to an array of highly disparate conditioning and triggering processes, including precipitation, frost
35 weathering, insolation, seismic activity, and slope modification (Collins and Stock, 2016; Rosser and Massey, 2022). In
36 Yosemite Valley, California, for example, rockfall triggers include rainfall events, snow melt, and freeze-thaw action that
37 can increase pressure along joints (Stock et al., 2011; Wieczorek and Jäger, 1996). Furthermore, rockfalls in Yosemite
38 Valley may also be triggered on warm summer days by cyclic solar heating, which can propagate exfoliation fractures and
39 lead to detachment (Collins and Stock, 2016). In the European Alps, warming and permafrost degradation have been
40 implicated in significant increases in rockfall activity (Allen and Huggel, 2013; Bajni et al., 2021; Bodin et al., 2015;
41 Paranunzio et al., 2015, 2016). Despite significant progress in characterizing rockfall triggering mechanisms, prediction of
42 rockfall timing and location has limited ability to inform warning systems (Rosser and Massey, 2022). Precursory rock
43 deformation can signal future activity (Abellán et al., 2010; Rosser et al., 2007; Royán et al., 2014), but current methods to
44 quantify precursor deformation across extensive areas composed of steep, high-relief surfaces are limited and oftentimes
45 rockfall occurs without prior deformation (Abellán et al., 2011). As a result, identifying rock slopes with the propensity to
46 generate rockfall, often referred to as rockfall source areas, is a key first step in mitigating rockfall hazards.

47

48 A wide array of methods has been proposed to assess the extent to which hillslopes are prone to rockfall activity. Delineating
49 potential source zones (e.g., Loye et al., 2009) can be accomplished from direct observation of past events, which assumes
50 the location of past detachments coincides with the likely location of future rockfall activity (Luckman, 1976; Matsuoka and
51 Sakai, 1999; Rapp, 1960; Whalley, 1984). Source zones can also be inferred from distinctive evidence such as talus and
52 scree deposits that have accumulated below cliff faces (Borella et al., 2019; Frattini et al., 2008; Moore et al., 2009; Stock
53 and Collins, 2014). Coupled assessment of rock slope morphology and the properties of potential source zones is another
54 common approach that uses digital elevation models (DEMs) for assessing source zones over large areas (Frattini et al.,
55 2008; Guzzetti et al., 2003; Messenzehl et al., 2017; Samodra et al., 2016), while more data-intensive and physically-based
56 deformation models can be used for slope-scale analyses (Matasci et al., 2018). In the absence of rock structure data, some
57 studies (e.g., Guerriero et al., 2024) have applied morphologic criteria (e.g., slope and curvature thresholds) to DEMs to
58 identify anomalous rock slope protrusions that are likely to experience rockfall events (Aksoy and Ercanoglu, 2006; Frattini
59 et al., 2008; Guzzetti et al., 2003; Marquínez et al., 2003; Sarro et al., 2024). Taken together, these studies suggest that the
60 approach to rockfall characterization is highly dependent on the availability of data, expansiveness of the study area, and the
61 desired level of confidence.

62

63 Because rockfall is typically localized along bedding planes, fractures, or joints, collectively referred to as discontinuities,
 64 susceptibility can also be evaluated by determining the geometry of these planes of weakness with respect to the slope and
 65 orientation of rock slopes. Kinematic analysis identifies blocks that can experience instability according to sliding, toppling,
 66 or wedge failure criteria as determined by the geometry of rock slopes and discontinuities (Fig. 1) (Bovis and Evans, 1996;
 67 Wyllie and Mah, 2004). Combining high-resolution DEMs with rock structure data can inform kinematic analyses and
 68 determine the relative likelihood of different failure modes across extensive study areas (Grant et al., 2016; Günther, 2003;
 69 Kundu et al., 2023; Meentemeyer and Moody, 2000; Stock and Collins, 2014). Recent applications of kinematic analysis
 70 leverage lidar or photogrammetry to extract bedrock discontinuity data and test kinematic failure criteria on complex slope
 71 geometries, like overhanging rock quarries (Fanos and Pradhan, 2018; Gigli et al., 2022). Increasingly, the acquisition of
 72 discontinuity data is accomplished using automated analysis of point cloud data acquired from terrestrial laser scanning
 73 (TLS) (Matasci et al., 2018) or lidar or photogrammetry acquired from uncrewed aerial systems (UAS) (Utlu et al., 2023).
 74 These approaches are powerful but can be challenging to implement across large areas characterized by steep, rocky forested
 75 slopes where the details of rock structure are often obscured by vegetation.



76

77 Figure 1. Schematic and corresponding stereonet representations of common rock slope failure modes: (a) planar sliding, (b)
 78 wedge, and (c) toppling. On the stereonet plots, the rock slope face orientation is represented by a solid black line, and poles

79 to planar discontinuities that meet conditions for failure are shown in shaded contours. Dashed lines represent planes of these
80 discontinuities. Modified from Wyllie and Mah (2004).

81

82 Initially, rock fragments move via creep, sliding, toppling, or falling before traveling downslope by following ballistic paths,
83 sliding, and rolling across rocky or talus slopes until stopping when sufficient energy dissipation has occurred via impacts
84 and/or friction (Caviezel et al., 2021). Computational rockfall runout models that account for the physics of these rockfall
85 processes can estimate the trajectories and kinetic energy of falling rocks to determine potential downslope impacts (Dorren
86 et al., 2007; Lu et al., 2021; Scheidl et al., 2020). Many DEM-based tools exist with a range of parameterization options to
87 perform physically-based rockfall simulations and predict the path of rocks over complex terrain and across variable land
88 cover (Lu et al., 2021; Moos et al., 2021). These models have been successfully employed to mitigate rockfall hazards with
89 diversion and attenuation structures, development setbacks, signage, or other means, in a variety of settings, including mines
90 and national parks (Guerriero et al., 2024; Klimeš et al., 2024; Stock and Collins, 2014; Stoffel et al., 2024). As a result, the
91 risk associated with rockfall activity can be reduced even though accurate prediction of triggering events remains elusive
92 (Rosser and Massey, 2022).

93

94 Although rockfall activity occurs in a wide range of geologic and climatic settings, it is particularly commonplace in post-
95 glacial landscapes owing to glacial erosion that alters near-surface stresses, fracture density, topographic variations from
96 glacial erosion, and changes in environmental conditions that occur in the wake of retreating glaciers (Ballantyne, 2002;
97 Leith et al., 2014). In particular, the spatial pattern of glacial erosion can align with the fabric of bedrock discontinuities and
98 set up failure-prone conditions across extensive areas. As such, relatively small changes in the orientation and geometry of
99 glacial valleys relative to the orientation of discontinuities can result in significant and systematic variations in rockfall
100 susceptibility. Although rockfall runout susceptibility is often simulated, the terrain characteristics that govern why and
101 where rockfall events tend to propagate long distances and pose risks downslope are seldom quantified. As a result, geologic
102 and geomorphic controls on rockfall hazard potential are typically not well understood, which prevents us from addressing
103 basic research and applied hypotheses such as how the magnitude and frequency of events accumulate and contribute to
104 mountain-scale erosion and how post-glacial slope morphology affects the efficacy of mitigation efforts (Barlow et al., 2012;
105 Corominas et al., 2014; Hales and Roering, 2007; Hungr et al., 1999; Moore et al., 2009; Rosser and Massey, 2022).

106

107 Rockfall activity is common across much of Southeast Alaska but has been particularly acute in the Municipality of
108 Skagway, which is situated in a narrow, glacially carved valley herein referred to as the ‘Skagway River valley’ and hosts
109 vigorous cruise ship tourism from late spring to early fall. Indigenous knowledge of avalanches in the area has been
110 established (Thornton, 2010) and documentation of rockfall activity in Skagway by colonial settlers began in the late 1800s
111 when gold prospecting fuelled the establishment of the town. Following decades of sporadic activity, several large rockfall

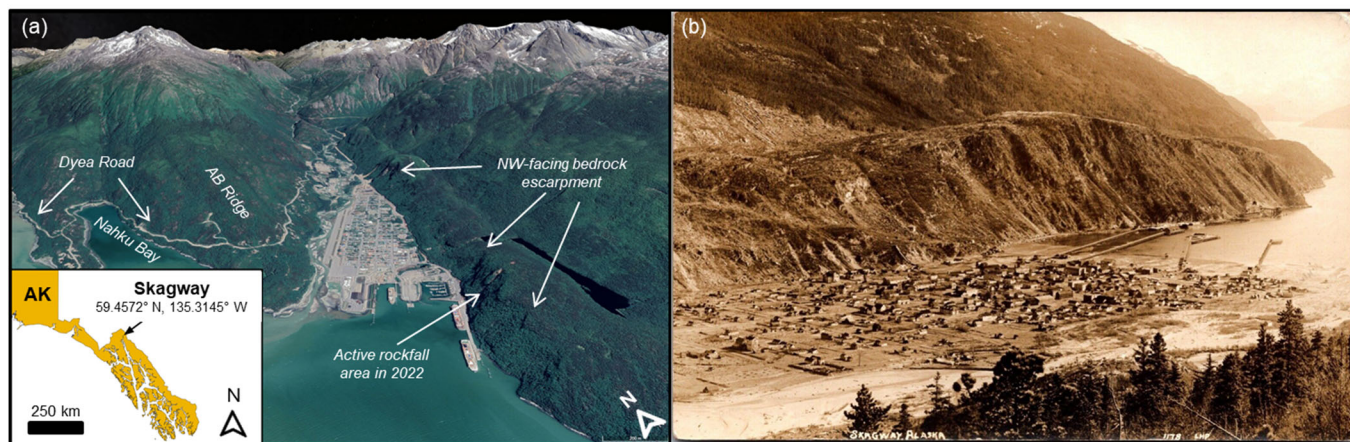
112 events in summer 2022 impacted cruise docks along Skagway Harbor and generated renewed concern about the extent and
113 scope of rockfall hazards in the area. In particular, the extent and timing of past rockfall activity is not well known and the
114 susceptibility of rockfall initiation and runout in the area, and particularly along a ~5km long ridgeline that abuts the harbour,
115 town centre, and railroad, has not been characterized. This study area affords an opportunity to explore novel approaches to
116 combining kinematic and runout models to assess how glacial erosion and bedrock properties modulate the spatial pattern of
117 rockfall hazard. In this contribution, we summarize a rockfall inventory and geologic data that reflects the distribution and
118 timing of past rockfall activity, document rock structure data from field observations, and synthesize new and existing lidar
119 data from airborne and UAS platforms to inform an integrated kinematic analysis susceptibility and dynamic runout model.
120 Our findings establish the pervasive imprint of rockfall activity along slopes oriented to promote toppling failure and
121 demonstrates how slope morphology determines rockfall propagation susceptibility. We highlight how the pattern of glacial
122 erosion resulted in substantial rockfall erosion and cliff retreat along favourably oriented slopes while unfavourably oriented
123 slopes experienced minimal modification since glacial retreat. Our integrated mapping and modelling approach suggests that
124 postglacial feedbacks between rock structure and hillslope evolution can generate strong variability in potential rockfall
125 impacts and thus inform current mitigation efforts and anticipate future needs.

126 **2 Study area: Skagway, SE Alaska**

127 **2.1. Geology and glacial history**

128 Near the northern extent of the Alaska Panhandle, Skagway is situated in the Taiya Inlet atop deltaic and fluvial deposits
129 near the outlet of a deep fjord (Fig. 2). The surrounding terrain is steep and rugged, composed of Tertiary granodiorite of the
130 Coast Range Batholith, a belt of plutonic and metamorphic rocks that extends to northern Washington (Yehle and Lemke,
131 1972). Deformation in southeastern Alaska and southwest Yukon is governed by the subduction and translation of
132 the Pacific-Yakutat plates relative to the North American plate in the St. Elias region (Biegel et al., 2024). The Eastern
133 Denali Fault and the Chatham strait fault lineaments, both strike-slip fault systems, meet just south of Skagway (Choi et al.,
134 2021). Deformation associated with these structures appears to impart a significant influence on the orientation of glacial
135 valleys, as fjords in the area tend to be linear, striking north and northeasterly (Yehle and Lemke, 1972). A dam
136 reconnaissance study focused on West Creek, a drainage just 9 km northwest of Skagway, identified three joint sets in the
137 granodiorite bedrock, including two abundant sets with northeast-strike and vertical or steep dips to the south, and one less
138 abundant set with northwest-strike and a consistent vertical dip (Callahan and Wayland, 1965). That study also noted the
139 coincident orientation of topographic lineations in the area and the strike of joints interpreted to be splays from the Chatham
140 strait lineament, which is related to the nearly 3,000-km long Denali fault system. Spacing between the joints is variable,
141 ranging from 1 to 4 meters, and the joints do not exhibit slickensides or cataclastic fabric (Fig. 3a-c). Sheeting joints in
142 granodiorite observed near the tops of glaciated ridges are slightly curved or irregular, tend to parallel the ground surface,
143 and spaced from 1 to 2 meters apart at the surface. Regional studies of glacial history imply that the most recent episode of

144 major glacial retreat and valley exposure in Skagway occurred 10 to 12kya (Baichtal et al., 2021; Menounos et al., 2017) and
145 icefields persist today in nearby inland valleys. The steep slopes around Skagway are generally devoid of glacial till owing to
146 post-retreat erosion and deposition in valley floors in the form of alluvial fans and colluvial deposits.



147 Figure 2. Study area. (a) Oblique view looking N-NE into Skagway River valley, Alaska. Note active rockfall along the NW-
148 facing ridgeline and escarpment above the harbour and cruise ship docks. Use of Google Earth ©2025 permitted for non-
149 commercial use. (b) Oblique view from AB Ridge looking SE across Skagway towards the NW-facing ridgeline and
150 escarpment. This undated and uncredited historic image postdates the late 1890s construction of the current Skagway City Hall
151 and Museum (photo provided by A. Beierly). Local steep cliff faces with fresh bedrock exposure signify active rockfall. Note
152 the lack of vegetation and the sharp bedrock escarpment along the crest of the ridgeline and the abundance of active talus
153 slopes that connect to the harbour.



155 Figure 3. Images (a, b) of open joints and incipient toppling along the bedrock escarpment on the NW-facing ridgeline above
 156 Skagway Harbor. (c) Image of joint orientations along shore of Nahku Bay. (d) Schematic of toppling prone hillside with
 157 opening joints and talus accumulation modified from Wyllie and Mah (2004). Photos a, b, and c by Ian Wachino and Josh
 158 Roering.

159 2.2. Climate and vegetation

160 Currently, Skagway experiences a subarctic maritime climate, characterized by cool summers and cold, snowy winters.
 161 Current average summer temperatures range from 10 to 21°C, with occasional rainfall, and winter temperatures range from -
 162 12 to -1°C, with heavy snowfall, and freezing conditions (Western Regional Climate Center, 2025). High winds that funnel
 163 up the Taiya Inlet are common and for decades it was reported that Skagway's name originated from Lingít words describing
 164 north winds (Thornton, 2010) although recent research concludes that the name derives from a contraction of 'Áa
 165 Wushigagu Ye', which translates as "the Place with Solid Core Trees" (X. Twitchell, pers. comm, 2024). Compared to other
 166 areas in SE Alaska, Skagway receives relatively low annual precipitation (mean annual precipitation is 1.1m) owing to the
 167 rain shadow imposed by the bounding coastal ranges to the south (Daly et al., 2018). Atmospheric rivers account for nearly
 168 70% of annual rainfall in Skagway and intense precipitation associated with these phenomena occur with highest frequency
 169 and intensity from August to October (Nash et al., 2024). Skagway hosts a coastal rainforest of spruce (*Picea sitchensis*),
 170 pine (*Pinus contorta*), and cedar (*Chamaecyparis nootkatensis*) trees with dense underbrush at low elevations (under 1,000m
 171 above sea level) and high-alpine tundra above tree line (Harris and Farr, 1974). Historical photographs and descriptions
 172 suggest that forests covering the slopes perched above Skagway Harbor and township were disturbed through timber harvest
 173 and burning in the early 1900s (Wright et al., 2021).

174

175 **2.3. Historic rockfall activity**

176 Early Western descriptions of rockfall activity in Skagway tend to focus on impacts to the harbour and railroad, including a
177 series of events in 1901 that recorded burial of the tracks near the approach to the wharf (The Daily Alaskan, 1901). The
178 location of this event coincides with the steep rocky slopes above Skagway Harbor, which have generated numerous
179 rockfalls since that account (Fig. 2). A study of geologic hazards in Skagway noted the striking linearity of N- and NE-
180 oriented fjords and valleys and identified abundant actively eroding bedrock escarpments on a NW-facing ridgeline that
181 coincides with a zone of historic rockfall activity adjacent to the township and harbour (Yehle and Lemke, 1972).
182 Downslope of these escarpments are colluvial deposits, consisting of landslide deposits, including talus from historic rockfall
183 events. The abundance and extent of these deposits implies significant slope adjustment and retreat since glacial retreat and
184 the relative activity of the deposits is reflected by the relative abundance of vegetation cover (Ruffner and Abrams, 1998;
185 van Steijn, 2002). Across the valley on the western side of Skagway, these talus deposits are much less prevalent, and the
186 Yehle and Lemke (1975) maps do not indicate the presence of erosional escarpments.

187

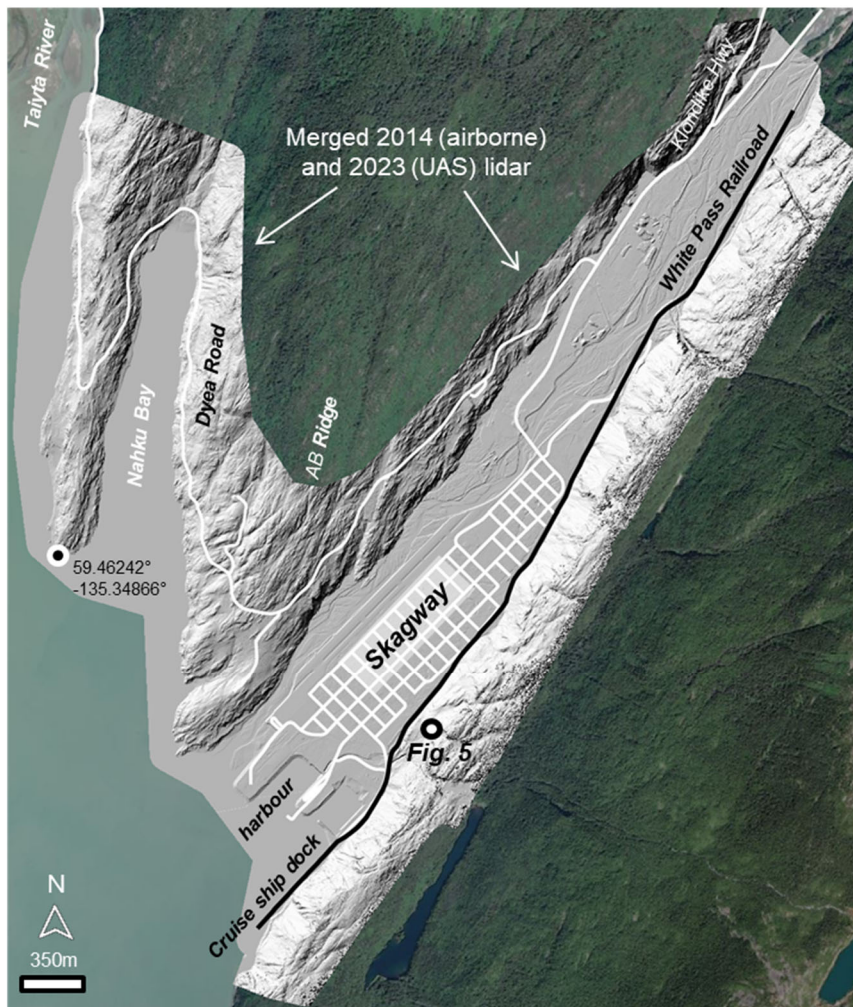
188 Rockfall hazard mitigation in the area is currently focused on the active rockfall source areas above the cruise ship dock in
189 Skagway Harbor. On June 23, 2022, rocks detached from the eastern ridgeline and impacted the cruise ship dock where
190 pedestrian traffic is frequent (Munson, 2022b). Two more rockfall events originating in the rocky slopes above the harbour
191 followed in rapid succession on August 3 and 5, 2022 (Munson, 2022a). Engineering efforts have been completed, which
192 include wrapping rock mesh covers over source areas, installing attenuator nets to block falling rocks, and scaling loose
193 rocks (Brennan and Whistler, 2022). Instrumentation has been installed to monitor the source area, including extensometers
194 installed at the top of the slope, which show that movement in the slide mass has increased from 4 cm per year to 6.5 cm per
195 year as of 2022 (Brennan and Whistler, 2022). Notably, the small section of rocky slopes above Skagway's cruise ship dock
196 is a small fraction of the roughly 5-km long stretch of ridgeline that borders the eastern margin of Skagway. Rocky
197 escarpments and talus deposits have been noted along the entire ridge (Yehle and Lemke, 1972), including the "Cemetery
198 Slide", a rockfall source area and runout zone stripped of vegetation by falling debris, which is similar to the active source
199 areas above the cruise ship dock. Although these zones of localized activity are well known, forest cover obscures the
200 geologic and topographic signature of past rockfall activity along the remainder of the ridge such that the pattern of relative
201 susceptibility and runout remains ambiguous.

202 **3 Methods**

203 **3.1. Overview**

204 Motivated by renewed rockfall activity, this study seeks to identify areas susceptible to rockfall initiation and runout within
205 the steep, post-glacial valleys around Skagway. Our analysis extends to the west of Skagway along Dyea Road to the Taiya

206 River, which hosts the Lingit settlement of Dyea and the Chilkoot Trailhead. Dyea Road is a well-travelled corridor that also
207 provides the opportunity to test our methodology across a wider range of topographic and structural configurations (Fig. 4).
208



209 Figure 4: Location map of Skagway, Nahku Bay, and Dyea Road showing a merged hillshade image of the 2014 airborne and
210 2023 UAS lidar bare earth data. White lines denote roads and the thick black line denotes a section of White Pass Railroad and
211 cruise ship dock used for our rockfall runout susceptibility analyses. The 2023 UAS lidar data was acquired along the ridge
212 southeast of the railroad while the 2014 airborne lidar accounted for the remainder of the study area imagery shown here.
213 Location of Figure 5 is shown by black/white filled dot. Background image from USGS NAIP (National Agriculture Imagery
214 Program).

215 3.2 Rockfall inventory

216 To investigate controls on rockfall timing, we accessed data generated for rockfall events between 2005 and 2022 from the
217 GeoEvent Slope Stability Database generated by the Alaska Department of Transportation & Public Facilities

218 (AKDOT&PF) Geotechnical Asset Management Program (Thompson, 2017). This database includes AKDOT&PF
219 maintenance and operations reports, including the location, date, event type (e.g., debris flows, rockfalls, landslides, snow
220 avalanches, flooding), relative magnitude, and cost, of slope processes that impact the Alaska highway system. Notably, this
221 database does not include information for activity along the White Pass Railroad that abuts the rockfall-prone ridgeline along
222 the eastern margin of Skagway. Nonetheless, it includes 866 rockfall event reports along segments of Skagway-Dyea Road
223 and Klondike Highway within our study area (Figure 4) that enabled us to assess climatic controls on rockfall activity. We
224 aggregated rockfall events according to Julian day to investigate seasonal trends in activity over the 17-yr record. For climate
225 context and comparison, we accessed Skagway Airport (PAGY) mean daily rainfall and mean daily maximum and minimum
226 temperature data for 2005 to 2025 (Horel et al., 2002).

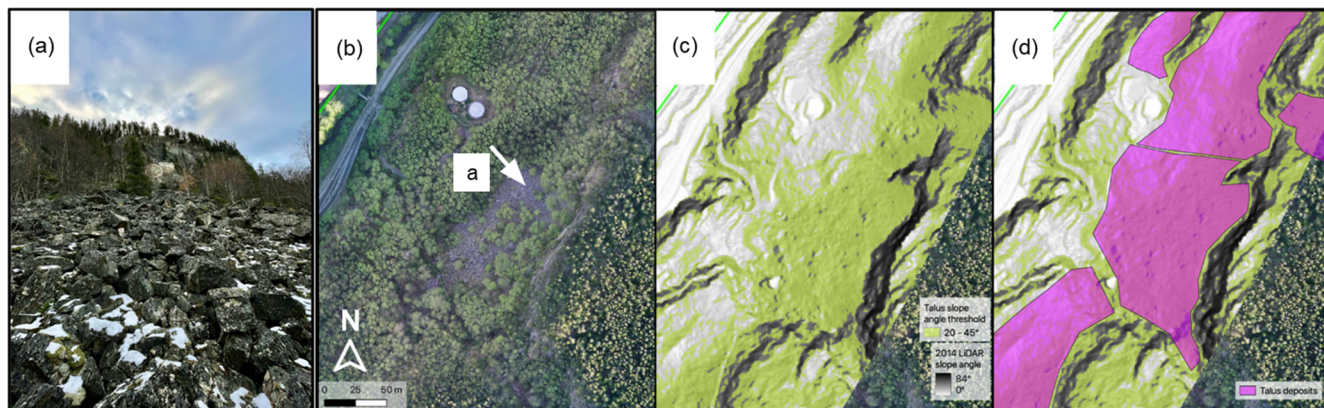
227 **3.3 High-resolution topography: Airborne and UAS lidar**

228 Our analysis used two sources of lidar data to inform geomorphic and bedrock mapping, kinematic analysis, and runout
229 modelling. We used a 2014 airborne lidar dataset with an average ground classified point density of 4.6 m⁻² acquired by the
230 Alaska Department of Geological and Geophysical Surveys (DGGS Staff, 2013) which includes low-elevation terrain in the
231 Skagway River valley, Nahku Bay, and part of Dyea valley (Macpherson et al., 2014). Because this lidar acquisition does not
232 span a significant portion of Skagway's rockfall-prone east ridge that abuts the township and harbour, we conducted a UAS
233 lidar survey in 2023 (Fig. 4). We acquired lidar data across the 2.3 km² area with peak elevations of 220 m near the cruise
234 ship docks and 320 m near the northern extent of the ridgeline (Roering et al., 2025). For the acquisition, the NSF RAPID
235 facility used a Trinity F90+ fixed wing drone with a Qube 240 lidar payload to fly ~120m above ground with 90% coverage
236 overlap. The surveyed area was slightly abbreviated due to a patch of extremely steep terrain where the UAS could not be
237 flown safely at distances sufficiently close to the ground surface to acquire data. The UAS survey produced a point cloud
238 containing 650 million total points with 200 million ground classified points, giving an average ground point density of 43
239 m⁻². We used the ground points to create a 1 m DEM using Cloud Compare (version 2.12.3) and combined it with the 2014
240 airborne lidar data to provide a continuous lidar coverage for our analyses (Fig. 4).

241 **3.4 Geomorphic mapping**

242 We used field observations, historic photographs, and slope thresholds and surface texture from the combined lidar DEM to
243 identify and map talus deposits that reflect the accumulation of rockfall deposits. These talus deposits include both forested
244 and unforested occurrences. To define the characteristic slope angles associated with active talus slopes we measured slope
245 angles from 20° to 45° that coincide with mapped talus deposits along the eastern ridge. Slopes steeper than 45° tend to
246 correspond with bedrock cliffs and outcrops, whereas slopes gentler than 20° often reflect relatively uneroded bedrock
247 surfaces or deposits from fluvial or other mass wasting processes. The relatively smooth texture of accumulated rockfall
248 deposits identified with hillshade and slopeshade layers (Burns and Madin, 2009) was also used to identify active talus
249 slopes as well as bedrock cliffs or outcrops that constitute a rockfall source area. Talus deposits occur on a wide range of

250 scales and for this analysis we focused on mapping patches of talus with area $>100\text{m}^2$ to ensure accuracy and highlight zones
251 of significant activity (Fig. 5). Specifically, we identified terrain that exhibits the relevant slope values as well as surface
252 textures consistent with talus deposits and then mapped polygons that enclose these zones when their areas exceeded 100m^2 .
253 The polygons were often separated by bedrock outcrops, gullies, and anthropogenic features.
254
255



256 Figure 5: Field images and lidar mapping of talus mantled slopes. (a) View looking SE along an exposed talus deposit with
257 boulder sized blocks at the base of a 40 m cliff known as Kirmse’s Cliff (lat: 59.45251, long: -135.31147), (b) Aerial imagery
258 from 2023 UAS survey showing a talus deposit and bedrock cliff, white arrow shows view direction for a, (c) Terrain within
259 the slope angle range of 20° - 45° colored in light green, and (d) map of talus polygons (pink) generated from lidar slope shade
260 and slope angle maps and orthoimagery. Hillshades in c and d derived from 2023 UAS lidar data. Background image from
261 USGS NAIP (National Agriculture Imagery Program).

262 3.5 Bedrock structure and discontinuities

263 To quantify the geometry of joints and discontinuities that contribute to rockfall initiation, we collected 405 structural
264 measurements (specifically, the strike and dip of planes that define the interfaces) at nearly 50 locations within the study area
265 and combined them to generate a comprehensive discontinuity dataset (Kundu et al., 2023). The steep, forested, and uneven
266 terrain surrounding Skagway limits access to outcrops and the traditional ‘scanline’ method (Priest and Hudson, 1981) was
267 untenable. Furthermore, the significant forest cover and expansiveness of the study area precluded the use of ground-based
268 laser or SfM (structure from motion) methods for acquiring structural information. Instead, we traversed the base of outcrops
269 as an approximation of scanlines and measured the orientation of planar surfaces expressed in the outcrop with
270 FieldMoveClino, a digital compass-clinometer smartphone app (Oliinyk et al., 2020), which enabled rapid and accurate data
271 acquisition. Our measurements were acquired across a wide range of locations in the study area to characterize spatial
272 variations in discontinuity orientations. In particular, we visited outcrops along the eastern, southern, and western corners of

273 the study area to ensure that the full range of relevant joint orientations was represented (Terzaghi, 1965). We identified joint
274 clusters by converting the strike and dip of discontinuity planes to poles on stereonet plots and used contouring to separate
275 different clusters (Wyllie and Mah, 2004).

276 **3.6 Kinematic analysis of rockfall susceptibility**

277 To assess the spatial pattern of rockfall susceptibility across the study area, we adopted a kinematic analysis approach with
278 our discontinuity data and applied criteria for planar sliding and toppling failure within our combined lidar DEM. This
279 approach foregoes the mechanical complexity and extensive parameterization of more sophisticated analyses (e.g., Matasci
280 et al., 2018) in order to generate results that span an extensive area. Kinematic analysis requires discontinuity data that is
281 locally representative. Traditionally, discontinuity measurements are taken in the field, whereas many modern applications
282 extract discontinuity orientations from high-resolution point clouds of the rock slope face (Utlu et al., 2023). Field
283 measurements remain a reliable and relevant means to capture joint orientations (Kundu et al., 2023), especially in locales
284 where terrestrial laser scans are not feasible due to hazardous terrain or where slope faces are obscured by vegetation.
285 As described below, the remarkable consistency of discontinuity orientations across the study area inspired this approach and
286 therefore we invoked the entire distribution of measured joint orientations at all locations to perform the kinematic analysis.
287 Specifically, we applied the stability criteria for each failure mode at each pixel in the merged lidar DEM by estimating the
288 fraction of the 405 joint orientations that are predicted to be unstable given the topographic aspect and slope angle of that
289 pixel. The failure criteria for planar and toppling failure are defined following Wyllie & Mah (2004) and described below.
290 Essentially, this approach is equivalent to locally performing a stereonet analysis of rock slope failure across our study area
291 and aggregating the results to identify potential rockfall failure modes and areas of high relative susceptibility. For the
292 analysis, we used a friction angle of 40°, consistent with measured values for jointed granodiorite similar to Skagway's
293 lithology (Alejano et al., 2019). To assess the accuracy of our modelled rockfall susceptibility maps, we visually compared
294 our predictions to the location of recent rockfall events in Skagway, as well as mapped bedrock cliffs and talus deposits,
295 which serve as a proxy for prior rockfall activity (Loye et al., 2009; Stock and Collins, 2014). In addition, we compared the
296 downslope direction of talus deposits with the aspect of topple-prone slopes to assess their relative correspondence.

297
298 Planar slides occur when the inclination of a bedrock slab exceeds the friction angle and it slides along a planar
299 discontinuity. Toppling failures occur when discontinuities steeply dipping into the rock slope face form slabs or columns of
300 rock that rotate forward along a fixed base (Fig. 1). Two types of toppling failures can occur that are influenced by the
301 strength of the rock mass and the geometry of discontinuities. Flexural toppling, where slabs of rock bend forward until they
302 break in flexure, is typical in shale and slate where orthogonal jointing is not well developed. Block toppling is common in
303 crystalline bedrock with orthogonal joint sets, where two steeply dipping joint sets form the sides of blocks, and a third set of
304 low angle, widely spaced joints form a basal failure plane. The active rockfall source area situated above Skagway's cruise
305 ship dock has been described as a progressive toppling failure with a stair-stepped basal feature (Brennan and Whistler,

306 2022). Topple failures observed in the field are consistent with this description, which is described by the block toppling
307 failure mechanism. As a result, our analysis focuses on block toppling and planar sliding given that field observations and
308 geotechnical reports do not identify wedge failures as a prevalent mechanism of rock slope instability. The challenge of
309 implementing multiple discontinuity orientations required for wedge analyses across our entire study area also encouraged us
310 to focus on block toppling and planar sliding in our analyses.

311
312 The criteria for planar, wedge, or toppling failure is based on the orientation of discontinuities and their orientation relative
313 to the rock slope face (Wyllie and Mah, 2004). The dip direction of the discontinuity (A) and rock slope (f) is given by α_A
314 and α_f , respectively, and the dip angle of the discontinuity and rock slope, both relative to horizontal, is given by ψ_A and ψ_f ,
315 respectively. The friction angle of the joint interfaces is given by ϕ .

316
317 Accordingly, a rock slope is susceptible to planar sliding failure along a discontinuity if the following three conditions are
318 simultaneously met:

$$319 \quad |\alpha_A - \alpha_f| < 20^\circ ; \psi_A < \psi_f ; \psi_A > \phi \quad (1)$$

320 The first condition requires that the interfaces are aligned in a sufficiently similar orientation (in this case within 20°) while
321 the second ensures that the discontinuity dip is shallower than the angle of the bedrock slope such that the discontinuity
322 intersects or ‘daylights’. The third and final condition demands that the interface slope angle exceeds the angle of friction. All
323 three conditions must be met at a given location for planar sliding to be deemed likely.

324
325 For block toppling failure, the following two conditions must be met simultaneously:

$$326 \quad \alpha_f - 20^\circ < (\alpha_A \pm 180^\circ) < \alpha_f + 20^\circ ; (90^\circ - \psi_f) + \phi < \psi_A \quad (2)$$

327 The first condition asserts that the discontinuity must dip into the rock slope face and be parallel, or nearly parallel (e.g., within
328 20°), to the dip direction of the slope face. The second condition indicates that the discontinuity dip must exceed the friction
329 angle allowing for interlayer slip between the blocks. In our model, the maximum allowable dip direction deviation is $\pm 20^\circ$
330 for both planar slide and block toppling failure. Although this value is sometimes chosen to be $\pm 10^\circ$ for block toppling we
331 expanded the constraint to $\pm 20^\circ$ (Cruden, 1989; Gigli et al., 2022).

332
333 Using equations 1 and 2, we estimated the number of joints in our field-derived dataset (n=405) that are predicted to exhibit
334 planar and toppling failure, respectively, for each pixel in our merged lidar DEM. Also, by simultaneously accounting for
335 both modes of potential failure at a given location it is possible to assess the combined susceptibility to toppling and planar

336 sliding although we do not formally account for this possibility in our analysis. Our maps of planar and toppling failure are
337 then calculated as the percentage of joints that meet the conditions required for failure conditions at each pixel in our study
338 area. For example, a toppling failure index value of 0.21 for a given pixel in our DEM indicates that 21% of the joints in our
339 joint dataset satisfy the two conditions in equation 2. This approach provides a description of relative rockfall initiation
340 susceptibility across our study area.

341 **3.7 Rockfall runout modelling with RAMMS**

342 To model potential runout paths associated with rock slopes that have high rockfall susceptibility, as determined by our
343 kinematic analyses, we used the 3D rockfall simulation software RAMMS:Rockfall (<https://ramms.ch/ramms-rockfall/>) to
344 represent the sliding, bouncing, and rolling motion of blocks as well as the internal, gravitational, and contact forces of a
345 rigid body that can translate and rotate. This model accounts for the energy balance of falling rocks and has been used
346 extensively at a range of scales for both applied and fundamental research studies (e.g., Caviezel et al., 2021; Kleinn et al.,
347 2024; Leine et al., 2014; Lu et al., 2019; Ringenbach et al., 2023). The primary inputs required for the RAMMS:Rockfall
348 model include digital elevation data (i.e., DEM), the location of rockfall source areas, specification of ground cover, and the
349 shape and size of the falling blocks.

350

351 We used our merged lidar DEM, which has a 1x1 m pixels and spans the area shown in Fig. 4. To identify potential source
352 areas, we identified pixels in our maps of toppling susceptibility with values greater than 5%. Pixels with >5% toppling
353 susceptibility demarcate rocky cliffs situated above our mapped talus deposits as well as areas of recent rockfall activity in
354 the Skagway Harbor (Fig. 5). The pixels with a >5% high toppling susceptibility were converted to polygons and only
355 polygons with area greater than 25 m² were retained to eliminate local high-relief features like boulders and trees that can
356 perpetrate the signature of rockfall source zones. Rockfall source points for RAMMS modelling were randomly distributed
357 across the resulting polygon coverage with a density of 0.04 m⁻² and a minimum point spacing of 5 m. This methodology
358 follows convention used in other studies (Lu et al., 2021) and yielded 4,945 rockfall initiation points for each of our
359 simulation scenarios.

360

361 The slopes east of Skagway are heavily forested, except in locations where falling debris has stripped vegetation, such as the
362 cruise ship dock and at the northern extent of the eastern ridge bordering Skagway. In RAMMS, we represented forested
363 areas as spruce alpine forests and trees were simulated in these areas using the ‘dense forest’ category in RAMMS, which is
364 defined by a stem density of 600 trees per hectare with a mean diameter of 30 cm. These parameters were chosen based on
365 our field observations and the typical density of mixed red alder coniferous stands in Southeast Alaska (Poage et al., 2007).
366 The effect of trees in the RAMMS rockfall runout module is to attenuate energy and reduce velocity, thus constituting a
367 significant impact on hazard potential. We mapped the distribution of trees by visually assessing the USGS NAIP imagery as
368 well as our UAS orthoimagery. The small amount of terrain (less than 5% of the study area) that exists outside these forested

369 areas was set to the fine talus cover category in RAMMS, which reflects negligible ground cover atop relatively fine-grained
370 talus deposits consistent with our field observations. We performed simulations with two land cover scenarios: 1) dense
371 forest and 2) fine talus cover, assigned across the entire simulation area to assess the potential role of timber harvest and fire
372 on rockfall runout and provide a conservative assessment of the hazard extent.

373

374 We estimated representative block size and shape by measuring the major axes of randomly selected blocks in exposed talus
375 piles (Hales and Roering, 2007). To estimate representative block sizes, the intermediate axis of 74 blocks was measured
376 from field measurements and high-resolution point clouds combined with orthoimagery. We determined the mean
377 intermediate axis size to be 1.08 m while the 50th percentile was 0.66 m and the 95th percentile was 3.56 m. Blocks observed
378 in the field are typically tabular and the characteristic geometry of blocks was estimated by measuring the long, intermediate,
379 and short axes of 10 blocks with sufficient exposure to allow measurement using our UAS-derived point clouds. We applied
380 the characteristic aspect ratio to the 50th percentile and 95th percentile intermediate axis values from our measurements. The
381 dimensions of the resulting rocks used in the simulation were 0.94 m x 0.66 m x 0.37 m (medium, 50th percentile), and 5.10
382 m x 3.56 m x 1.99 m (large, 95th percentile), which represent moderate and large block sizes, respectively. Given the
383 tendency for large blocks to travel longer distances, our 95th percentile blocks are intended to reflect the conservative (or
384 long runout) scenario (Statham, 1976). For these simulations, we assumed rock density of 2,700 kg m⁻³.

385

386 To simulate the range of potential rockfall impacts, we focused on four scenarios for RAMMS simulation with the following
387 parameterizations: 1) 50th percentile block with fine talus cover, 2) 50th percentile block with dense forest, 3) 95th percentile
388 blocks with fine talus cover, and 4) 50th percentile block with dense forest. To account for the stochastic nature of rockfall
389 release, we used RAMMS to select 1 of 10 randomly chosen block orientations to be released at each source point, yielding
390 49,450 individual rockfall runout paths for each of the four scenarios. Our results presented here focus on the two end-
391 member scenarios (50th percentile with dense forest cover and 95th percentile with fine-grained talus over) to illustrate the
392 range of rockfall behaviour.

393

394 For our runout analysis, we focused on the eastern NW-facing ridgeline of the Skagway River valley to assess potential
395 impacts to the harbour and township. We used an array of analyses to investigate rockfall runout patterns and topographic
396 controls on the runout behaviour. First, to identify terrain with high likelihood of rockfall runout we used RAMMS to
397 calculate the number of rockfall events that traversed each pixel in our model domain for each of the scenarios. As such, the
398 cumulative number of rockfall passages at each pixel accounts for both the abundance of upslope source areas as well as the
399 tendency for topography to steer or direct rockfall into particular pathways. Second, we used RAMMS to create a “digital”
400 boundary (or barrier) coincident with the railroad tracks along the base of the ridgeline to record rockfalls that bypass the
401 boundary and have the potential to impact the harbour and township. Third, to estimate how topographic properties moderate
402 rockfall runout, we calculated local slope and terrain roughness across the simulation domain. Roughness was calculated as

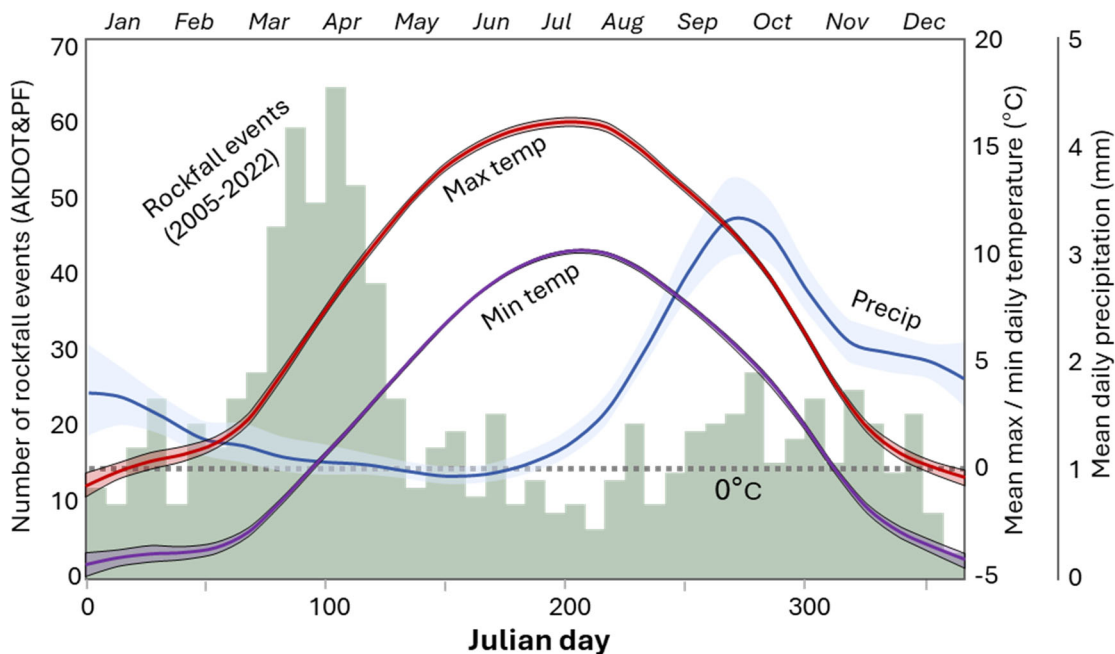
403 the standard deviation of local slope values within a 5-m radius window. This approach has been successfully used to
 404 differentiate the kinematics and age of landslide deposits (Booth et al., 2017; LaHusen et al., 2020) and in this case, we
 405 choose the 5-m scale to be consistent with the scale of blocks, fractures, and bedrock landforms. Finally, we generated a 5.4-
 406 km long transect coincident with the railroad within our simulation domain to quantify along-ridge variations in rockfall
 407 passages, upslope source areas, slope angle, and terrain roughness.

408 4 Results

409 4.1 Rockfall inventory

410 The AKDOT&PF database includes 866 reports of rockfall-related maintenance and operation activities along the 10.3-km
 411 long segment of Skagway-Dyea and Klondike Hwy within our study area between 2005 and 2022 (Fig. 6,7). This implies an
 412 average rockfall frequency of 50 events per year, although this value is an overestimate because some of the reports are
 413 redundant given that multiple days are reported in response to a single event. Among the events, 7 resulted in road closures
 414 that lasted 3 days or longer in March 2012, October 2012, January 2014, March 2015, February 2016, September 2016, and
 415 December 2020.

416



417 Figure 6. Analysis of seasonal variation in rockfall activity and climate variables from the AKDOT&PF geoevent database
 418 (2005-2022) and daily mean precipitation and daily maximum and minimum temperature from the Skagway Airport
 419 (PAGY) for the period 2005-2025. The number of rockfall events (green bars) exhibits seasonal variations that don't

420 obviously align with precipitation (blue) although maximum temperature (red) and minimum temperature (purple) increase
421 significantly during the typical period of rockfall activity in March and April. The horizontal dashed grey line represents
422 freezing. The confidence intervals for the climate data represent standard error of mean values over the period of record.

423

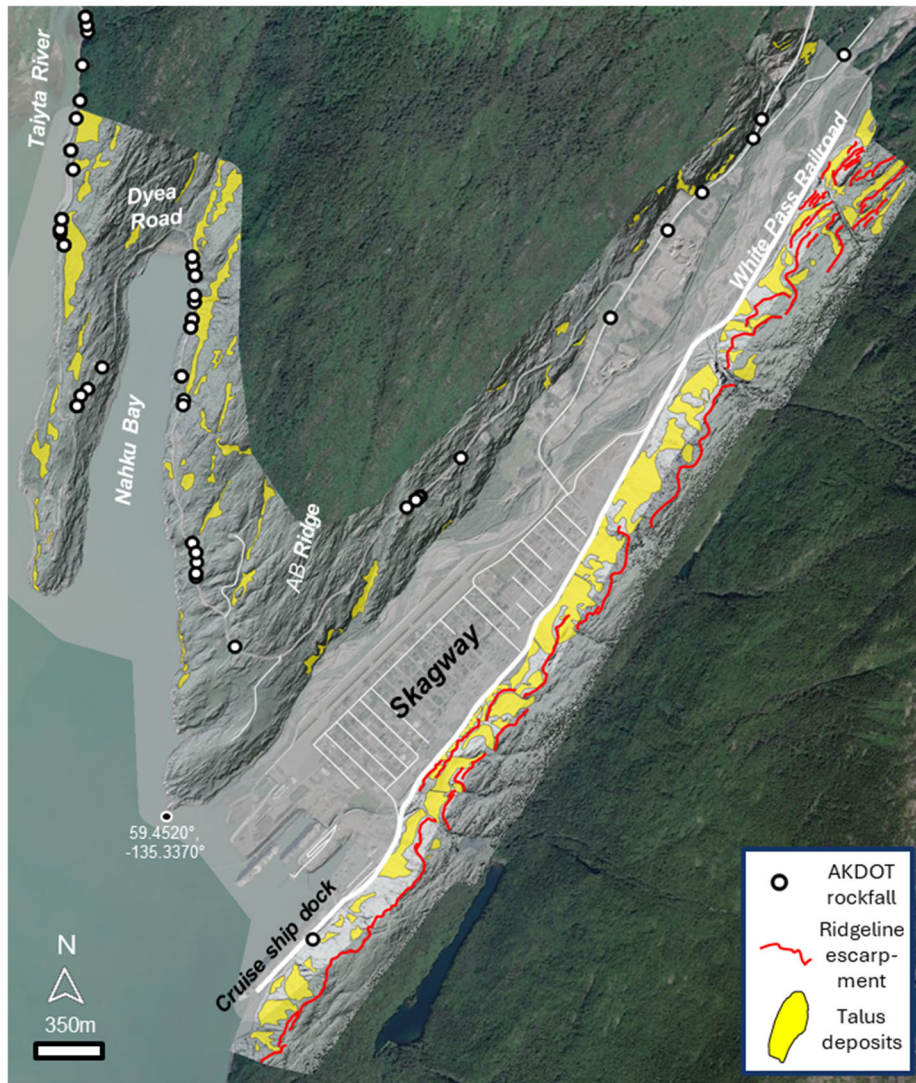
425 According to our analysis, rockfall events peak in late March and April, occurring at a pace that is 4x greater than the
426 remainder of the year (Fig. 6). This substantial uptick in activity corresponds with a seasonal increase in daily temperatures,
427 particularly when the minimum daily temperature exceeds zero. This implies that thawing of frozen rock slopes promotes the
428 destabilization of blocks through the loss of tensile strength and increases in pore pressure from melting ice and snow. In the
429 fall, increased daily rainfall associated with atmospheric rivers with a detectable but small increase in activity. The mid-
430 summer period of warm temperatures and dry conditions corresponds with the least active period. Some notable high impact
431 rockfall events correspond with intense rainfall events, including December 2, 2020, when widespread events were preceded
432 by over 3 inches of rainfall in the previous 24 hours.

433 **4.2 Geomorphic mapping**

434 The morphology of glaciated valleys around Skagway is variable owing to bedrock structure, differential glacial erosion, and
435 post-glacial landscape evolution (Fig. 4). These factors generate systematic variations in the abundance of bedrock cliffs that
436 serve as rockfall source areas as well as long, steep slopes that facilitate long rockfall runout. On the east side of Skagway
437 River valley, our lidar DEM and field observations reveal a distinct northwest-facing bedrock escarpment that runs parallel
438 just below the crest of the ridgeline (Fig. 7). This feature is particularly distinct above the cruise ship dock, where the
439 ridgeline has high relief compared with sections to the north that abut the township. Below these bedrock escarpments, we
440 observe abundant talus deposits that extend continuously downslope to the base of the ridgeline and the valley floor (Fig. 7).
441 An undated historic photograph which postdates the 1899 construction of the current Museum and City Hall depicts the
442 eastern ridgeline in a state of minimal forest cover such that the escarpment and talus slopes above the harbour are clearly
443 visible (Fig. 2b). These observations imply substantial post-glacial erosion through lateral (southeastward) retreat of the
444 ridgeline as talus slopes convey bedrock downslope creating long and relatively smooth pathways for rockfall runout. In
445 Figure 2b, the ridge on the left side of the image exhibits gentler slope angles ($<20^\circ$) and a benchy morphology which
446 implies less extensive post-glacial erosion and slope modification via rockfalls. Atop the ridge and east of the escarpment,
447 the ridgeline contains abundant evidence of unmodified glacial erosion features (Figure 4).

448

449 By contrast, the west side of the Skagway River valley has a very different morphology, in that it lacks a distinct escarpment
450 and instead exhibits consistent and gradual slopes that imply minimal post-glacial modification. Locally, we observe vertical
451 cliffs along the Skagway River, but otherwise the west side of the Skagway River valley consists of gentle rock slopes that
452 form prominent ridges and parallel the strike of the valley. We observe a similar pattern of bedrock escarpments and talus
453 deposits along the NW-facing slopes of two parallel ridgelines between Skagway and the Taiya River (Fig. 7).



455 Figure 7: Distribution of talus deposits (yellow polygons), AKDOT&PF rockfall geoevents (2005-2022) (white/black dots),
 456 and Eastern ridge bedrock escarpment (red lines). Note the abundance of talus deposits on the NW-facing ridgeline in Skagway
 457 and on NW-facing slopes in Nahku Bay and along Dyea Road. Background image from USGS NAIP (National Agriculture
 458 Imagery Program). Merged lidar hillshade image has 50% transparency.

459

460 Our lidar and field mapping revealed abundant talus slopes on northwest-facing ridgelines across our study area. More
 461 generally, talus deposits compose 12% of the 7.2 km² total mapped area (Fig. 7). Along the eastern ridgeline, we identified
 462 abundant talus slopes which collectively make up 25% of that ridgeline area. On the west side of the Skagway River valley,
 463 the southeast-facing ridgeline hosts sparse talus cover that constitutes only 3% of that side of the valley. Similarly, talus
 464 deposits on the southeast-facing ridgelines bordering Nahku Bay are much less abundant (1%) and smaller in area than on the

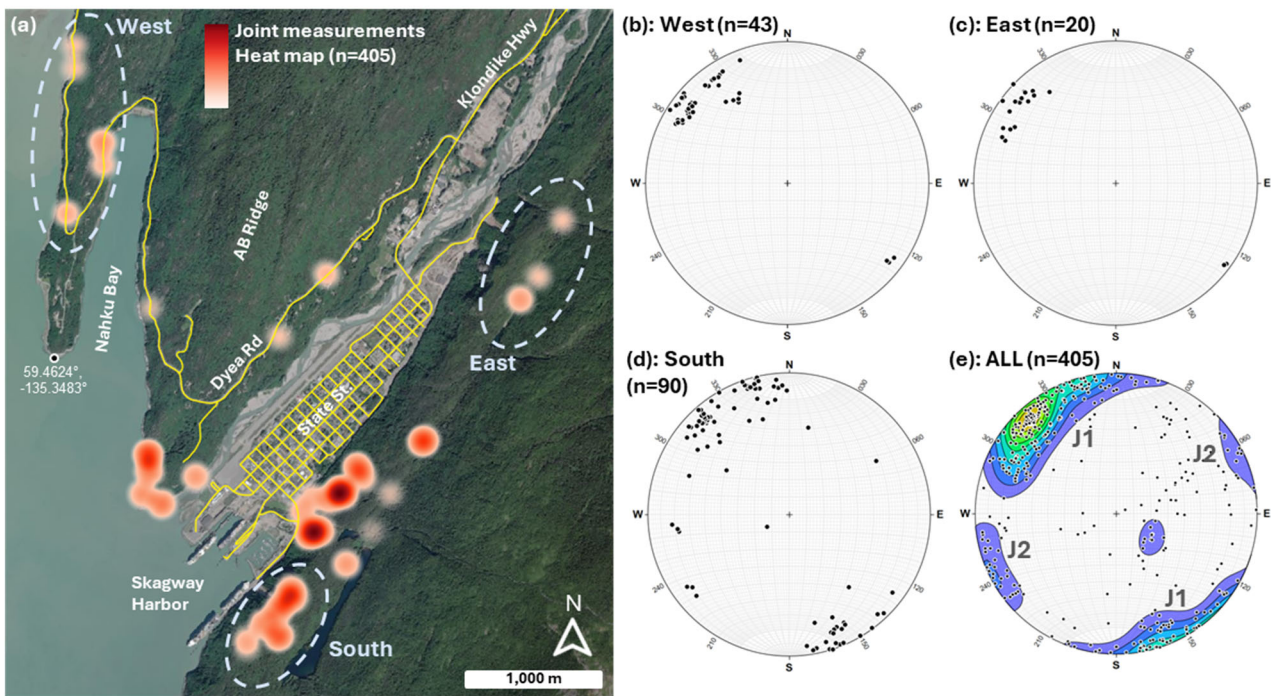
465 northwest-facing ridgeline that abuts the bay (11%). In summary, talus slopes are significantly more abundant on NW-facing
466 slopes across our study area and their location tends to correspond with AKDOT&PF geoevents along Dyea Road (Fig. 7).

467 4.3 Bedrock structure and discontinuities

468 To characterize the geometry of discontinuities with the potential to generate rockfalls, we collected 405 joint orientations
469 from 48 granodiorite outcrops across the study area (Fig. 8a, supplemental materials) and plotted the data as poles to planes
470 on an equal area stereonet to identify dense clusters of poles which were then grouped into joint sets (Fig. 8b-e). Two
471 dominant joint sets were identified in this survey (*J1* & *J2*), which are steeply dipping and approximately orthogonal (Fig.
472 8e). The steeply dipping joints are conducive to toppling, which is the most observed failure mode in Skagway. The most
473 densely defined joint set is *J1*, which parallels the strike of the lower Skagway River valley and the eastern ridgeline and
474 predominantly dips to the southeast. The less densely defined joint set (*J2*), is approximately orthogonal to *J1*, has near
475 vertical dips, and strikes northwest.

476
477 We subsampled the joint orientation data in three geographic zones at the corners of our study area in order to assess the
478 consistency of the rock structure. Joint orientations from the western portion of the study area are remarkably similar to those
479 observed in the eastern and southern sections of our study area (Fig. 8b-d). This finding supports our use of the same
480 bedrock structure data for kinematic analysis across the entire study area.

481

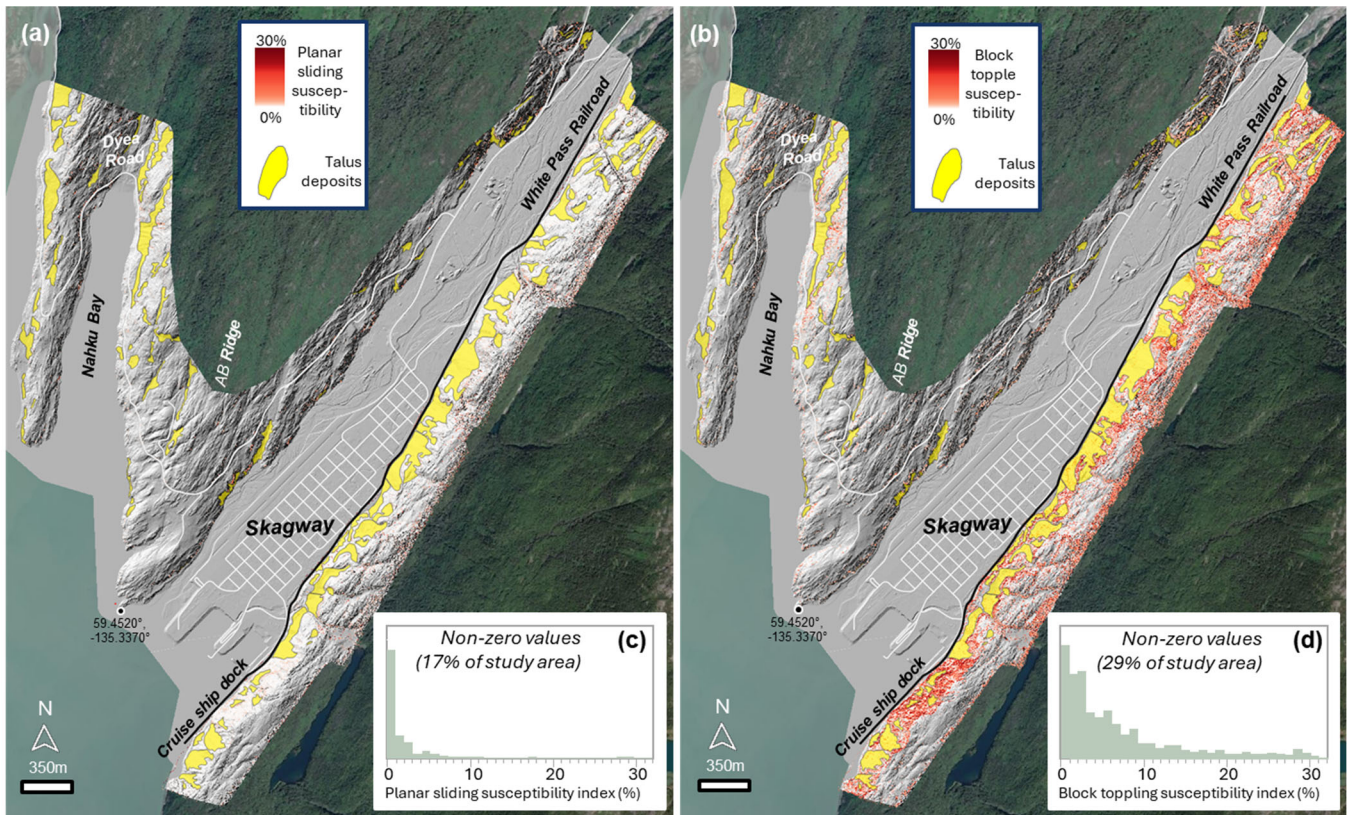


482 Figure 8: Joint survey data. (a) Location of 405 structural measurements from 48 outcrop locations with heat map showing
483 relative abundance and dashed ellipses showing subsampled data shown in panels b-d. (b-e) Lower hemisphere equal area
484 stereonet plots of joint measurements visualized as poles to planes for West (b), East (c), South (d), and ALL joint data (e).
485 The plot in e shows Kamb contours to highlight dense clusters of poles (warm colors reflect high density and cool colors
486 convey low density) and two dominant joint sets (J1 and J2) are labeled. Background image in (a) from USGS NAIP (National
487 Agriculture Imagery Program).

488

489 **4.4 Kinematic analysis of rockfall susceptibility**

490 By combining equations 1 and 2 with our joint orientation data (Fig. 8) and merged lidar dataset (Fig. 4), we mapped
491 susceptibility to planar sliding and block toppling, respectively, across our study area (Fig. 9a,b). Terrain susceptible to
492 planar failure is sparse and 83% of the terrain has zero values of susceptibility such that none of the measured joint
493 orientations satisfy the planar sliding criteria. Furthermore, the terrain with non-zero planar sliding susceptibility values has
494 very low values with a small fraction exceeding 5% (Fig. 9c). By contrast, our analysis demonstrates that 29% of the terrain
495 has non-zero values of block toppling susceptibility and a substantial fraction of the non-zero values exceed 5% (Fig. 9d).
496 This result emerges because the abundance of consistently oriented joints with vertical or sub-vertical dips promotes block
497 toppling, which is supported by field observations. Furthermore, given the consistent orientation of sub-vertical joints across
498 our study area (Fig. 8), the primary control on rockfall susceptibility to toppling is the orientation and inclination of rock
499 faces according to equation 2. Along the ridge that borders the eastern margin of Skagway River valley, for example, the
500 glacially flattened bench at the ridge crest is not steep enough ($<20^\circ$) to meet topographic conditions for either failure mode
501 (Fig. 9a,b). Moving to the west side of the crest, however, the gentle ridgetop abruptly transitions to the steep escarpment
502 where overhanging, cliffy bedrock slopes are perched above extensive talus deposits (Fig. 7). In these locations, our analyses
503 show that a substantial portion ($>20\%$) of observed joints promote toppling failure (see deep red colours in Fig. 9b).
504 Furthermore downslope, we observe patchy zones of high toppling susceptibility, many of which are in close proximity to
505 Skagway township and harbour. Along the southeast-facing rock slopes that border the west side of Skagway, our analyses
506 show few and small patches of terrain with toppling susceptibility approximating 5%, indicating low susceptibility. This
507 asymmetric susceptibility pattern continues along the sub-parallel ridges west of Skagway along Dyea Road with west- and
508 northwest-facing ridgelines exhibiting abundant patches of terrain with high propensity for toppling failure and east- and
509 southeast-facing slopes showing negligible toppling susceptibility (Fig. 9b). More generally, by combining our talus deposit
510 map with our toppling susceptibility map, we note a strong correspondence such that zones with $>5\%$ toppling failure tend to
511 occur just upslope of talus-mantled slopes (Fig. 9b). Furthermore, our maps show that zones with values of toppling
512 susceptibility less than 5% tend to be more isolated and less clearly connected with talus deposits. As a result, the 5%
513 toppling susceptibility index value serves as an effective threshold for defining rockfall source areas.



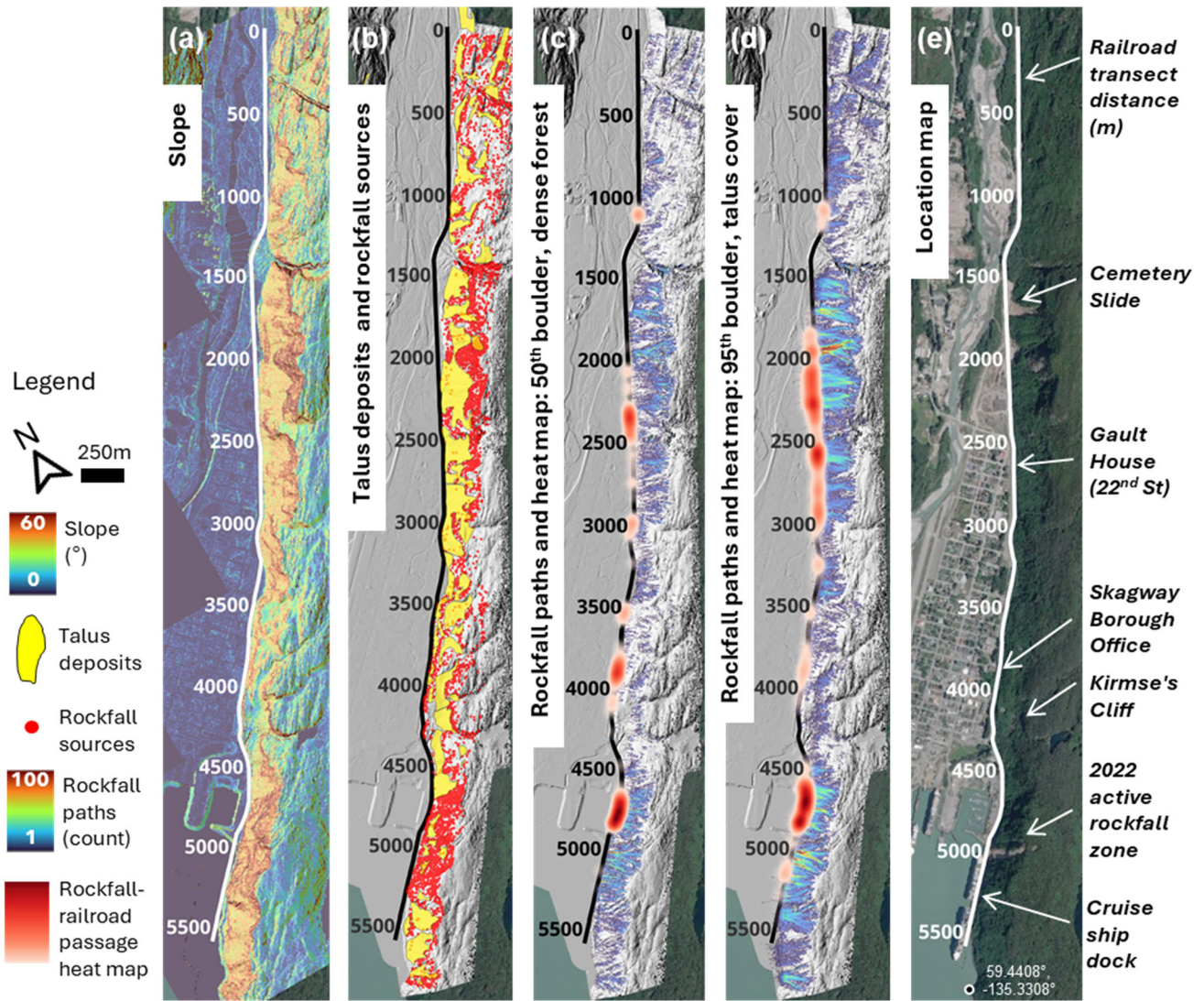
514 Figure 9: Maps of (a) planar sliding and (b) block toppling susceptibility indices using combined 2014 airborne and 2023
 515 UAS lidar datasets and joint orientation data. Histograms of (c) planar sliding and (d) block toppling susceptibility indices
 516 for non-zero values. The mapped and plotted values are the percentage of field-surveyed joints deemed unstable at each pixel
 517 according to equations 1 (planar sliding) and 2 (block toppling). Yellow polygons denote talus deposits. Note the abundance
 518 of toppling failure zones on NW-facing rock slopes that border Skagway and Nahku Bay as well as the correspondence
 519 between toppling susceptibility and talus deposits. Hillshade imagery derived from combined 2014 and 2023 lidar data.
 520 Background image from USGS NAIP (National Agriculture Imagery Program).

521

522 4.5 Rockfall runout modelling using RAMMS

523 Using zones of high toppling susceptibility ($>5\%$) as source areas for rockfall initiation, we applied RAMMS to model the
 524 runout of 49,450 rockfall events for each of the four scenarios that account for differences in block size and ground cover.
 525 We applied the runout model along the ridge bordering the eastern margin of Skagway and used the 5.4-km long section of
 526 the White Pass Railroad extended along the cruise ship dock to demarcate rockfall passages with potential impact to the
 527 harbour and township (Fig. 10a-e). The ridge is steeper in the southern (4500 to 5500 m on the railroad transect) and central
 528 (1500 to 3000 on the transect) sections where extensive bedrock cliffs protrude above talus deposits (Fig 10a). These cliffs

529 are identified as zones of high toppling susceptibility and thus designated as rockfall source areas (Fig. 10b). Our simulations
530 showing the number of rockfall events that pass through each pixel reveal distinct zones subject to high rockfall
531 susceptibility as well as extensive downslope transport (Fig. 10c,d). For both the 50th block/dense forest and 95th block/fine
532 talus scenarios shown here, the southern end of the ridgeline above the harbour (between 4500 and 5500 on the transect)
533 exhibits >10 specific chutes or paths of efficient rockfall runout whereby initiation near the escarpment results in the
534 concentration of rockfall runout along these paths and conveyance to the cruise ship docks and/or harbour. Both scenarios
535 exhibit a zone of events that pass across the railroad as depicted by the heat map (Fig 10c,d). In contrast, the central portion
536 of the ridgeline (between 3000 and 4500m on the transect) immediately adjacent to much of the township exhibits patchy
537 and less frequent rockfall activity along gentle and irregularly oriented bedrock steps and benches. Further north, our
538 simulations reveal abundant long rockfall runout paths at the northern extent of the township with concentrated activity near
539 the Cemetery Slide area (between 1500 and 3000m on the transect) with a high concentration of blocks predicted to pass
540 across the railroad (Fig 10d). Finally, at the northernmost extent of our simulation domain (from 0 to 1500m on the transect),
541 the results show patchy and short rockfall transport paths coincident with gentle, benchy topography. Taken together, these
542 simulations demonstrate a large fraction of the ridge has similar morphology and modelled rockfall runout behaviour as the
543 zone of recent activity above the cruise ship dock.
544



545

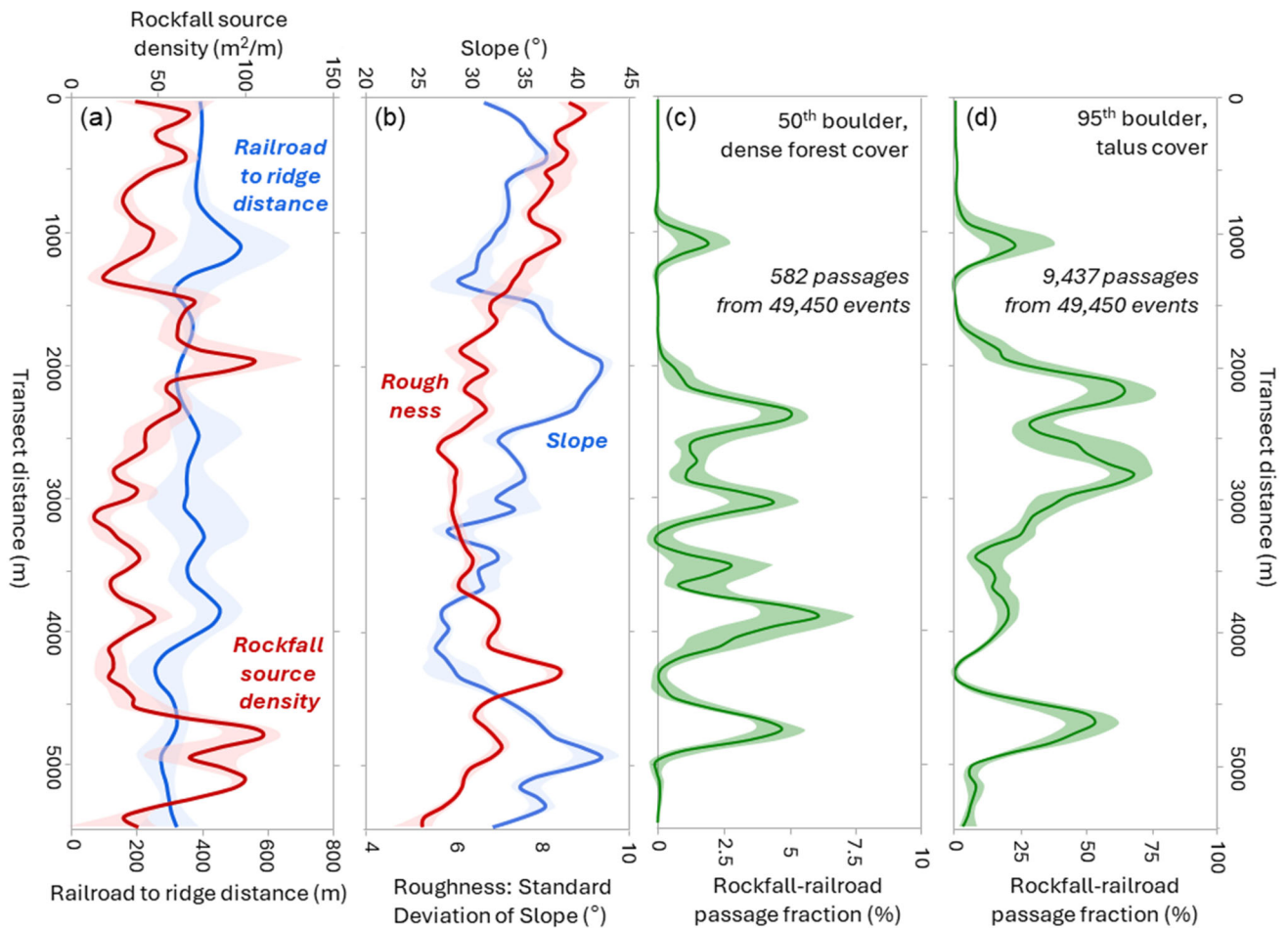
546 Figure 10: Map of topography and rockfall models along the ridgeline that abuts Skagway township and Harbor. (a) Map of
 547 slope angle using merged 2014 airborne and 2023 UAS lidar, (b) Map of rockfall sources (red points) and talus deposits (yellow
 548 polygons), (c, d) Maps of modeled rockfall paths for 2 scenarios with variable block size and land cover. The number of
 549 rockfall events that traverse each pixel is indicated by the color ramp. Heat map (red shades) denotes relative density of
 550 modeled rockfalls that pass over the railroad, (e) Satellite image from USGS NAIP (National Agriculture Imagery Program)
 551 with annotated locations indicated. All maps include railroad transect demarcations. Hillshade images in (b-d) derived from
 552 merged lidar datasets.

553

554 To assess controls on rockfall propagation susceptibility along the railroad transect, we tallied the number of simulated
555 rockfall events that traverse the railroad track and quantified topographic properties of the ridge (Fig. 11). Although the
556 railroad-to-ridge distance (or ridge width) is relatively consistent along the transect, the density of rockfall source areas
557 varies substantially (Fig. 11a). The southern section of the ridge (4500 to 5400m) has a concentration of toppling source
558 areas, which is ~4x higher than slopes in the central section (2500 to 4000m) of our transect. Another zone of high source
559 density occurs at ~2000m on the transect and values to the northern extent are low to moderate in magnitude. Average slope
560 angle along the ridge varies substantially with high values ($>35^\circ$) in the southern (4500 to 5400m) and north-central (1500 to
561 2500m) sections and low values in the south-central section (3000 to 4500m) (Fig. 11b). Average values of slope roughness
562 (estimated as the standard deviation of slope estimated for local windows with 5m radius) are relatively high in the southern
563 section of the transect and low in the central section before increasing monotonically to the north (Fig. 11b). Notably, our
564 analysis shows that slope angle, rockfall source density, and roughness exhibit distinctive patterns along the ridge enabling
565 us to distinguish their influence on the modelled runout pattern.

566
567 Although the relative pattern of simulated runout is consistent for the two scenarios shown here (Fig. 10c,d), our transect
568 analysis shows that only 1.2% of the simulated events for the 50th block/dense forest scenario result in passage across the
569 railroad whereas 19.1% of the 95th block/fine talus scenario events travel across the railroad (Fig. 11c,d). In several sections,
570 the passage fraction for the 95th block/fine talus scenario exceeds 50%, implying that the destabilization of a large block will
571 likely result in downslope impacts (Fig 11d). By contrast, the passage fractions for the 50th block/dense forest scenario rarely
572 exceed 4% such that unstable blocks have a low probability of impacting the valley (Fig 11c). This disparity reveals the
573 profound influence of block size and land cover on rockfall propagation susceptibility. Furthermore, the modelled runout
574 patterns reveal how slope morphology controls rockfall propagation. In both scenarios, sections of the ridge with high
575 passage fractions correspond with low roughness values and the zone of high roughness at 4000 to 4500m on the transect
576 corresponds with negligible rockfall passage (Fig 11b). By contrast, our analyses show that mean slope angle and rockfall
577 source density do not strongly correlate with the pattern of rockfall passage across the railroad.

578



579

580 Figure 11: Plots of rockfall model variables and topographic properties along the railroad transect that bisects Skagway and
 581 the rockfall prone ridgeline (see Figure 10 for location). (a) Profile of rockfall source density ($\text{m}^2 \text{m}^{-1}$), which depicts the
 582 upslope area of toppling-prone terrain (normalized by distance along transect) calculated with equation 2 for terrain between
 583 the railroad and the ridge crest, and plot of the horizontal distance between the railroad and ridge crest, (b) Profile of average
 584 slope and roughness (estimated as standard deviation of local slope within a 5-m radius window) for terrain between railroad
 585 and the ridge crest, (c) Profile of modeled rockfall-railroad passage percentage for the scenario with 50th percentile block size
 586 and dense forest cover, and (d) Profile of modeled rockfall-railroad passage percentage for the scenario with 95th percentile
 587 block size and fine talus land cover. Shaded intervals convey standard deviation of values in all plots.

588 **5 Discussion**

589 Although rainfall has been responsible for triggering some notable rockfall events in Skagway, a substantial seasonal
 590 increase in rockfall events documented in the AKDOT&PF inventory occurred in late March and April. This period
 591 corresponds to rapid increases in temperatures, particularly the minimum daily temperature, which implies that thawing of

592 ice, snow, and rock mass may contribute to increased activity (Fig. 6). This observation is consistent with many studies that
593 have documented thermal-driven rockfall activity in alpine environments in Europe and elsewhere; the proposed
594 mechanisms include active layer thaw, ice-filled fracture destabilization, and thermal stress cycles, with peak activity
595 typically occurring during spring and early summer months when temperatures rise above freezing (Draebing et al., 2022;
596 Gruber et al., 2004; Krautblatter et al., 2013; Matsuoka and Sakai, 1999; Mayer et al., 2024). Given that the low-elevation
597 rock slopes around Skagway are too warm to support permafrost, ice-filled fracture destabilization may be a relevant
598 mechanism. Field-based studies have noted cleft ice in rockfall scars which implies that ice segregation processes during
599 cold periods followed by warming and thaw-induced weakening can destabilize fractured rock masses (Huggel et al., 2012;
600 Ravelle et al., 2013). Dendrochronological studies in Switzerland reveal that 88% of rockfall scars occur between mid-
601 October and end of May, with peak activity in April when ice lenses formed from meltwater slowly infiltrate into fractures
602 (Stoffel et al., 2005). These studies highlight the critical role of spring thaw in destabilizing previously frozen rock masses
603 which may be relevant to the timing of rockfall activity in Skagway. Nonetheless, the specific timing of seasonal activity
604 remains challenging to predict, motivating efforts to determine the spatial pattern of rockfall initiation and propagation
605 susceptibility to mitigate hazard.

606

607 Taken together, our analyses of block toppling susceptibility and talus deposition maps demonstrate that rockfall source
608 areas and runout paths tend to be situated on northwest-facing rock slopes in the Skagway River valley, Nahku Bay, and
609 lower Taiya River valley. Our joint dataset suggests that this strong topographic control on rockfall activity owes to the
610 coincident alignment of glacial valleys and joint orientations, both of which are remarkably consistent in the area. The joints
611 measured in this study are consistent with the steeply dipping, orthogonal joint sets measured in a nearby (~15km northwest
612 of Skagway) structural survey in on a tributary to the Taiya River (Callahan and Wayland, 1965) and described in a
613 geotechnical assessment of the rock slopes above Skagway's cruise ship dock (Brennan and Whistler, 2022). These high
614 angle joints are likely formed by the tensile component of shearing from the nearby Chatham Strait fault and Eastern Denali
615 fault systems. Rock slopes with orthogonal jointing are often predisposed to block toppling failure particularly where steep
616 orthogonal joints form the sides of toppling blocks and low angle joints act as the basal failure plane (Wyllie and Mah,
617 2004).

618

619 The results of our kinematic analysis demonstrate that rock slopes in the steep rugged terrain surrounding Skagway are
620 highly susceptible to block toppling failure. The preference for toppling failure is due to the steep inclination of joints, which
621 are conducive to toppling failure as their near verticality tends to preclude them from daylighting in rock slope faces, a
622 necessary condition for planar sliding or wedge failure (Figure 1). The abundance of talus deposits situated just downslope
623 of zones with high toppling susceptibility (Fig. 9b) is consistent with other studies (Guerriero et al., 2024) and supports the
624 utility of our modelling approach. More advanced treatments that explicitly account for individual trees, land cover features,

625 and source block geometry would improve the local accuracy of our simulations although the regional-scale results presented
626 here are robust and helpful for informing mitigation efforts.

627

628 Consistent with previous studies (e.g., Loye et al., 2009), our rockfall susceptibility maps are consistent with the failure
629 mode and location of rock slope deformation observed in the field. On the uphill side of the prominent escarpment along the
630 eastern ridgeline in the lower Skagway River valley (Fig. 7), we observed numerous instances of detached parallel slabs of
631 rock separated by open tension cracks that extend downward for several meters (Fig. 3). These blocks appear to be
632 experiencing the early phases of toppling failure as vegetation and other environmental perturbations can contribute to crack
633 widening (Pawlik et al., 2016; Rempel et al., 2016). These observations also indicate that our predicted zones of toppling
634 failure are likely to continue propagating southeast with the active bedrock escarpment providing additional blocks to initiate
635 rockfall. More generally, these observations suggest that erosion and southeast-oriented lateral migration of the ridgeline has
636 been substantial since glacial retreat 10 to 12 kya. Approximate reconstruction of the ridge to its immediate post-glacial
637 geometry (Moore et al., 2009) implies that 10 to 100 meters of lateral erosion has occurred during the Holocene. The linear
638 character of the escarpment and pervasive indicators of active toppling also imply parallel retreat over geomorphic
639 timescales, which occurs given the favourable combination of dip and slope angle as well as erosion rate (Imaizumi et al.,
640 2015). As such, the unravelling and lateral retreat of the escarpment will likely continue until the interface encounters a
641 different configuration of slope and structural geometry.

642

643 As our simulations demonstrate, extensive rockfall activity and lateral divide migration does not occur along the entire ridge.
644 Rather, our results show large sections with patchy and localized talus deposits and benchy bedrock landforms that arises
645 because of variations in the depth and pattern of glacial erosion. On Kirmse's Cliff (at 4200m on the transect, Fig. 10e), for
646 example, talus deposits extend upslope from the valley floor to vertical cliff faces that terminate at the ridgeline (Fig. 5). In
647 this area, toppling susceptibility is relatively high, but concentrated in a relatively small area of vertical rock slope, and a
648 forested talus deposit and benchy zone sits between the cliff and the valley floor (Fig. 10b). By contrast, several areas along
649 the escarpment exhibit high potential for rockfall runout to reach the valley. At the cruise ship dock (4500m on the transect),
650 continuous, rockfall-prone slopes above the cruise ship dock span from the escarpment to the base of the slope, resulting in a
651 large area with high rockfall propagation susceptibility in close proximity to harbour infrastructure. Similarly, from 1500 to
652 2000m on our railroad transect, a high-relief escarpment with steep vertical bedrock outcrops near the crest exhibits a
653 continuous steep slope to the valley floor (Fig. 10a). In this area, which is the source area for the Cemetery Slide, rockfall
654 susceptibility and long runout potential are high and we observed frequent spalling and rolling rocks traversing the talus
655 deposits during our field work (Fig. 10c,d). In fact, The Daily Alaskan reported a 1914 rockfall event just south of the
656 Cemetery Slide at 2500m along the transect which coincides with our simulations of high rockfall runout potential (Figs.
657 10c,d). During that event, L. Gault noted “an avalanche of earth and stone” that “leaped the railroad track...pounding against
658 the fence.” Gault also noted that the railroad track served as a “safety barrier” because “the force of the descent had been so

659 much lessened.” Further afield in the northeast section of Nahku Bay, another zone of high rockfall susceptibility is revealed
660 by our analysis. Steep rocky slopes rise to an elevation of 250 m with close proximity to Dyea Road (Fig. 7). This area lacks
661 a well-developed runout path, but it does coincide with source areas for dozens of events in the AKDOT rockfall inventory
662 that impacted Dyea Road.

663

664 Our analyses reveal distinctive zones of high rockfall initiation and runout (or propagation) susceptibility in the Skagway
665 region that result from the combination of glacial erosion that sets the morphology of bedrock slopes and the orientation of
666 joint sets that determine the geometry of potential bedrock failures. Most likely, the orientation and extent of glacial erosion
667 is not independent of the joints (Hooyer et al., 2012; Krabbendam and Glasser, 2011). Rather, we suspect that the nearly
668 parallel orientation of joints and the N-NE trending ridge along the eastern margin of the Skagway River valley arise due to
669 glacial erosion tracking discontinuities that facilitate erosion more readily than undeformed bedrock. This long-term
670 evolution implies feedbacks between rock structure and bedrock erosion processes from glaciers and rockfalls that support
671 strong gradients in rockfall activity. In assessing how these factors moderate the current hazard context, our findings
672 critically depend on the combination of kinematic modelling and runout susceptibility to provide constraints for identifying
673 areas at risk to inform mitigation efforts. Additional work is needed, however, to conduct a rigorous characterization of
674 rockfall risk in Skagway that includes estimation of occupation and usage of structures and transportation corridors to be
675 coupled with our results (e.g., Michoud et al., 2012).

676 **6 Conclusions**

677 The integrated kinematic analysis and the runout modelling presented here matches well with field observations and provides
678 the basis for a sophisticated approach in rockfall hazard assessment. The steeply dipping orthogonal joints in Skagway’s rock
679 slopes are highly conducive to block toppling failure which has resulted in highly asymmetric rockfall susceptibility. Our
680 results highlight a distinct contrast in the morphology of Skagway River valley’s eastern and western ridgelines, which is
681 primarily determined by the predisposition of northwest-facing slopes to block toppling failure along a densely fractured
682 joint set that dips steeply to the southeast. This is consistent with geomorphic evidence of extensive rockfall activity, where
683 talus deposits are more abundant and larger on the eastern side of the lower Skagway River valley than the west. This
684 structural control on rockfall activity is also evident in the east and west sides of Nahku Bay, situated to the west of
685 Skagway. Our analysis of a rockfall inventory indicates a similar preference for initiating on northwest-facing slopes and
686 reveal a seasonal peak in rockfall activity in late March and April that likely results from thawing of ice-filled joints and
687 reduction of rock mass strength. Our simulations of rockfall runout show areas with high rockfall susceptibility that may
688 merit further investigation and mitigation: 1) the ridgeline and slopes above the cruise ship dock, 2) the high-relief
689 topography at the north end of Skagway, and 3) the eastern ridgeline bordering Nahku Bay. Recent rockfall source areas
690 located in these regions are characterized by steep northwest-facing slopes that are highly susceptible to block toppling

691 failure and reach >200 m in elevation which facilitates long runout paths. Our results also demonstrate that slope roughness
692 over ~10m scales serves as a better predictor of rockfall propagation than slope angle and the density of rockfall source areas.
693 Our integrated modelling approach and field assessment provides a simple but robust approach to assess rockfall hazard.

694 **7 Data availability**

695 All topographic data used for analyses are cited within the text. The structural data are available as Supplemental material.

696 **8 Author contribution**

697 IW and JR conceived and designed the study and IW and JR executed the study, RC provided on-site context, knowledge
698 and guidance, AP contributed to study design and fieldwork, IW and JR prepared the manuscript with contributions from all
699 other co-authors.

700 **9 Acknowledgments**

701 This research was funded by NSF Award #2052972 (Focused CoPe: Building Community Sensor Networks for Coastal
702 Hazards and Climate Change Impacts in Southeast Alaska), which supports community-driven fundamental and translational
703 geohazard science for project partners across SE Alaska. The authors thank leaders and members of the Skagway Traditional
704 Council and residents of Skagway for their observations, critical insights, hospitality, and field assistance; the Municipality
705 of Skagway for sharing rockfall reports; and the NSF-funded UW RAPID facility for the timely acquisition of UAS lidar
706 data. Conversations with Joe Wartman, Ben Leshchinsky, alex grant, Chris Massey, and Dimitrios Zekkos were insightful
707 and contributed to our understanding of rock slope processes.

708

709 **10 References**

- 710 Abellán, A., Calvet, J., Vilaplana, J. M., and Blanchard, J.: Detection and spatial prediction of rockfalls by means of terrestrial
711 laser scanner monitoring, *Geomorphology*, 119, 162–171, <https://doi.org/10.1016/j.geomorph.2010.03.016>, 2010.
- 712 Abellán, A., Vilaplana, J. M., Calvet, J., García-Sellés, D., and Asensio, E.: Rockfall monitoring by Terrestrial Laser Scanning
713 – case study of the basaltic rock face at Castellfollit de la Roca (Catalonia, Spain), *Natural Hazards and Earth System Sciences*,
714 11, 829–841, <https://doi.org/10.5194/nhess-11-829-2011>, 2011.
- 715 Aksoy, H. and Ercanoglu, M.: Determination of the rockfall source in an urban settlement area by using a rule-based fuzzy
716 evaluation, *Natural Hazards and Earth System Sciences*, 6, 941–954, <https://doi.org/10.5194/nhess-6-941-2006>, 2006.

- 717 Alejano, L. R., Veiga, M., Pérez-Rey, I., Castro-Filgueira, U., Arzúa, J., and Castro-Caicedo, Á. J.: Analysis of a complex
718 slope failure in a granodiorite quarry bench, *Bull Eng Geol Environ*, 78, 1209–1224, <https://doi.org/10.1007/s10064-017-1160->
719 [y](https://doi.org/10.1007/s10064-017-1160-y), 2019.
- 720 Allen, S. and Huggel, C.: Extremely warm temperatures as a potential cause of recent high mountain rockfall, *Global and*
721 *Planetary Change*, 107, 59–69, <https://doi.org/10.1016/j.gloplacha.2013.04.007>, 2013.
- 722 Baichtal, J. F., Lesnek, A. J., Carlson, R. J., Schmuck, N. S., Smith, J. L., Landwehr, D. J., and Briner, J. P.: Late Pleistocene
723 and early Holocene sea-level history and glacial retreat interpreted from shell-bearing marine deposits of southeastern Alaska,
724 USA, *Geosphere*, 17, 1590–1615, <https://doi.org/10.1130/GES02359.1>, 2021.
- 725 Bajni, G., Camera, C. A. S., and Apuani, T.: Deciphering meteorological influencing factors for Alpine rockfalls: a case study
726 in Aosta Valley, *Landslides*, 18, 3279–3298, <https://doi.org/10.1007/s10346-021-01697-3>, 2021.
- 727 Ballantyne, C. K.: A general model of paraglacial landscape response, *The Holocene*, 12, 371–376,
728 <https://doi.org/10.1191/0959683602hl553fa>, 2002.
- 729 Barlow, J., Lim, M., Rosser, N., Petley, D., Brain, M., Norman, E., and Geer, M.: Modeling cliff erosion using negative power
730 law scaling of rockfalls, *Geomorphology*, 139–140, 416–424, <https://doi.org/10.1016/j.geomorph.2011.11.006>, 2012.
- 731 Biegel, K. M., Gosselin, J. M., Dettmer, J., Colpron, M., Enkelmann, E., and Caine, J. S.: Earthquake Relocations Delineate a
732 Discrete Fault Network and Deformation Corridor Throughout Southeast Alaska and Southwest Yukon, *Tectonics*, 43,
733 e2023TC008140, <https://doi.org/10.1029/2023TC008140>, 2024.
- 734 Bodin, X., Schoeneich, P., Deline, P., Ravel, L., Magnin, F., Krysiński, J.-M., and Echelard, T.: Mountain permafrost and
735 associated geomorphological processes: recent changes in the French Alps, *Journal of Alpine Research | Revue de géographie*
736 *alpine*, <https://doi.org/10.4000/rga.2885>, 2015.
- 737 Booth, A. M., LaHusen, S. R., Duvall, A. R., and Montgomery, D. R.: Holocene history of deep-seated landsliding in the North
738 Fork Stillaguamish River valley from surface roughness analysis, radiocarbon dating, and numerical landscape evolution
739 modeling: Landsliding in the N. Fork Stillaguamish, *Journal of Geophysical Research: Earth Surface*, 122, 456–472,
740 <https://doi.org/10.1002/2016JF003934>, 2017.
- 741 Borella, J., Quigley, M., Krauss, Z., Lincoln, K., Attanayake, J., Stamp, L., Lanman, H., Levine, S., Hampton, S., and Gravley,
742 D.: Geologic and geomorphic controls on rockfall hazard: how well do past rockfalls predict future distributions?, *Natural*
743 *Hazards and Earth System Sciences*, 19, 2249–2280, <https://doi.org/10.5194/nhess-19-2249-2019>, 2019.
- 744 Bovis, M. J. and Evans, S. G.: Extensive deformations of rock slopes in southern Coast Mountains, southwest British
745 Columbia, Canada, *Engineering Geology*, 44, 163–182, [https://doi.org/10.1016/S0013-7952\(96\)00068-3](https://doi.org/10.1016/S0013-7952(96)00068-3), 1996.
- 746 Brennan, K. and Whistler, R.: Railroad dock landslide, initial site visit trip report, Skagway, Alaska,
747 *Geotechnical/Environmental Report*, No. 109508-001, Shannon & Wilson, Anchorage, AK, USA, 2022.
- 748 Burns, W. J. and Madin, I. P.: Protocol for Inventory Mapping of Landslide Deposits from Light Detection and Ranging (lidar)
749 Imagery, Oregon Department of Geology and Mineral Industries (DOGAMI) Special Paper 42, 36p., 2009.
- 750 Callahan and Wayland: Geologic reconnaissance of the West Creek damsite near Skagway, Alaska, *Geological Survey*
751 *Bulletin*, 1211-A, <https://doi.org/10.3133/b1211A>, 1965.

- 752 Caviezel, A., Ringenbach, A., Demmel, S. E., Dinneen, C. E., Krebs, N., Bühler, Y., Christen, M., Meyrat, G., Stoffel, A.,
753 Hafner, E., Eberhard, L. A., Rickenbach, D. von, Simmler, K., Mayer, P., Niklaus, P. S., Birchler, T., Aebi, T., Cavigelli, L.,
754 Schaffner, M., Rickli, S., Schnetzler, C., Magno, M., Benini, L., and Bartelt, P.: The relevance of rock shape over mass—
755 implications for rockfall hazard assessments, *Nat Commun*, 12, 5546, <https://doi.org/10.1038/s41467-021-25794-y>, 2021.
- 756 Choi, M., Eaton, D. W., and Enkelmann, E.: Is the Eastern Denali fault still active?, *Geology*, 49, 662–666,
757 <https://doi.org/10.1130/G48461.1>, 2021.
- 758 Collins, B. D. and Stock, G. M.: Rockfall triggering by cyclic thermal stressing of exfoliation fractures, *Nature Geoscience*, 9,
759 395–400, <https://doi.org/10.1038/ngeo2686>, 2016.
- 760 Corominas, J., van Westen, C., Frattini, P., Cascini, L., Malet, J.-P., Fotopoulou, S., Catani, F., Van Den Eeckhaut, M.,
761 Mavrouli, O., Agliardi, F., Pitalakis, K., Winter, M. G., Pastor, M., Ferlisi, S., Tofani, V., Hervás, J., and Smith, J. T.:
762 Recommendations for the quantitative analysis of landslide risk, *Bull Eng Geol Environ*, 73, 209–263,
763 <https://doi.org/10.1007/s10064-013-0538-8>, 2014.
- 764 Cruden, D. M.: Limits to common toppling, *Can. Geotech. J.*, 26, 737–742, <https://doi.org/10.1139/t89-085>, 1989.
- 765 Daly, C., Smith, J., and Halbleib, M.: 1981-2010 High-Resolution Temperature and Precipitation Maps for Alaska Final
766 Report, Oregon State University, Corvallis, Oregon, 2018.
- 767 DGGS Staff: LiDAR Datasets of Alaska, Alaska Division of Geological & Geophysical Surveys,
768 <https://doi.org/10.14509/25239>, 2013.
- 769 Dorren, L., Berger, F., Jonsson, M., Krautblatter, M., Mölk, M., Stoffel, M., and Wehrli, A.: State of the art in rockfall – forest
770 interactions, *Schweizerische Zeitschrift für Forstwesen*, 158, 128–141, <https://doi.org/10.3188/szf.2007.0128>, 2007.
- 771 Draebing, D., Mayer, T., Jacobs, B., and McColl, S. T.: Alpine rockwall erosion patterns follow elevation-dependent climate
772 trajectories, *Commun Earth Environ*, 3, 1–12, <https://doi.org/10.1038/s43247-022-00348-2>, 2022.
- 773 Fanos, A. and Pradhan, B.: Laser Scanning Systems and Techniques in Rockfall Source Identification and Risk Assessment:
774 A Critical Review, *Earth Systems and Environment*, 2, <https://doi.org/10.1007/s41748-018-0046-x>, 2018.
- 775 Frattini, P., Crosta, G., Carrara, A., and Agliardi, F.: Assessment of rockfall susceptibility by integrating statistical and
776 physically-based approaches, *Geomorphology*, 94, 419–437, <https://doi.org/10.1016/j.geomorph.2006.10.037>, 2008.
- 777 Gigli, G., Lombardi, L., Carlà, T., Beni, T., and Casagli, N.: A method for full three-dimensional kinematic analysis of steep
778 rock walls based on high-resolution point cloud data, *International Journal of Rock Mechanics and Mining Sciences*, 157,
779 105178, <https://doi.org/10.1016/j.ijrmms.2022.105178>, 2022.
- 780 Grant, A., Wartman, J., and Abou-Jaoude, G.: Multimodal method for coseismic landslide hazard assessment, *Engineering
781 Geology*, 212, 146–160, <https://doi.org/10.1016/j.enggeo.2016.08.005>, 2016.
- 782 Gruber, S., Hoelzle, M., and Haeberli, W.: Permafrost thaw and destabilization of Alpine rock walls in the hot summer of
783 2003, *Geophysical Research Letters*, 31, <https://doi.org/10.1029/2004GL020051>, 2004.
- 784 Guerriero, L., Annibali Corona, M., Di Martire, D., Francioni, M., Limongiello, M., Tufano, R., and Calcaterra, D.: Rockfall
785 susceptibility analysis of the “San Michele Arcangelo” historic trail (Central Italy) based on virtual outcrops and multiple
786 propagation models, *Bull Eng Geol Environ*, 83, 263, <https://doi.org/10.1007/s10064-024-03764-0>, 2024.

- 787 Günther, A.: SLOPEMAP: programs for automated mapping of geometrical and kinematical properties of hard rock hill slopes,
788 *Computers & Geosciences*, 29, 865–875, [https://doi.org/10.1016/S0098-3004\(03\)00086-4](https://doi.org/10.1016/S0098-3004(03)00086-4), 2003.
- 789 Guzzetti, F., Reichenbach, P., and Wieczorek, G. F.: Rockfall hazard and risk assessment in the Yosemite Valley, California,
790 USA, *Natural Hazards and Earth System Sciences*, 3, 491–503, <https://doi.org/10.5194/nhess-3-491-2003>, 2003.
- 791 Hales, T. C. and Roering, J. J.: Climatic controls on frost cracking and implications for the evolution of bedrock landscapes,
792 *Journal of Geophysical Research*, 112, <https://doi.org/10.1029/2006JF000616>, 2007.
- 793 Harris, A. S. and Farr, W. A.: The forest ecosystem of southeast Alaska: 7. Forest ecology and timber management., Gen.
794 Tech. Rep. PNW-GTR-025. Portland, OR: U.S. Department of Agriculture, Forest Service, Pacific Northwest Research
795 Station. 116 p, 025, 1974.
- 796 Hooyer, T. S., Cohen, D., and Iverson, N. R.: Control of glacial quarrying by bedrock joints, *Geomorphology*, 153–154, 91–
797 101, <https://doi.org/10.1016/j.geomorph.2012.02.012>, 2012.
- 798 Horel, J., Splitt, M., Dunn, L., Pechmann, J., White, B., Ciliberti, C., Lazarus, S., Slemmer, J., Zaff, D., and Burks, J.:
799 MESOWEST: COOPERATIVE MESONETS IN THE WESTERN UNITED STATES, 2002.
- 800 Huggel, C., Allen, S., Deline, P., Fischer, L., Noetzi, J., and Ravel, L.: Ice thawing, mountains falling—are alpine rock
801 slope failures increasing?, *Geology Today*, 28, 98–104, <https://doi.org/10.1111/j.1365-2451.2012.00836.x>, 2012.
- 802 Hungr, O., Evans, S. G., and Hazzard, J.: Magnitude and frequency of rock falls and rock slides along the main transportation
803 corridors of southwestern British Columbia, *Can. Geotech. J.*, 36, 224–238, <https://doi.org/10.1139/t98-106>, 1999.
- 804 Hungr, O., Leroueil, S., and Picarelli, L.: The Varnes classification of landslide types, an update, *Landslides*, 11, 167–194,
805 <https://doi.org/10.1007/s10346-013-0436-y>, 2014.
- 806 Imaizumi, F., Nishii, R., Murakami, W., and Daimaru, H.: Parallel retreat of rock slopes underlain by alternation of strata,
807 *Geomorphology*, 238, 27–36, <https://doi.org/10.1016/j.geomorph.2015.02.030>, 2015.
- 808 Kleinn, J., Christen, M., and Bartelt, P.: Probabilistic event-based rockfall modelling for deriving continuous intensity-
809 frequency curves in the impact area, *Interpraevent 2024. Conference proceedings*, 648–652, 2024.
- 810 Klimeš, J., Kilnar, J., Kopačková-Strnadová, V., Pánek, T., McColl, S., and Jelének, J.: Landslides in the glaciated mountains
811 of the Cordillera Blanca, Peru—types, spatial distribution, and conditioning factors, *Landslides*,
812 <https://doi.org/10.1007/s10346-024-02387-6>, 2024.
- 813 Krabbendam, M. and Glasser, N. F.: Glacial erosion and bedrock properties in NW Scotland: Abrasion and plucking, hardness
814 and joint spacing, *Geomorphology*, 130, 374–383, <https://doi.org/10.1016/j.geomorph.2011.04.022>, 2011.
- 815 Krautblatter, M., Funk, D., and Günzel, F. K.: Why permafrost rocks become unstable: a rock–ice-mechanical model in time
816 and space, *Earth Surface Processes and Landforms*, 38, 876–887, <https://doi.org/10.1002/esp.3374>, 2013.
- 817 Kundu, J., Sarkar, K., Ghaderpour, E., Mugnozsa, G. S., and Mazzanti, P.: A GIS-Based Kinematic Analysis for Jointed Rock
818 Slope Stability: An Application to Himalayan Slopes, *Land*, 12, <https://doi.org/10.3390/land12020402>, 2023.
- 819 LaHusen, S. R., Duvall, A. R., Booth, A. M., Grant, A., Mishkin, B. A., Montgomery, D. R., Struble, W., Roering, J. J., and
820 Wartman, J.: Rainfall triggers more deep-seated landslides than Cascadia earthquakes in the Oregon Coast Range, USA,
821 *Science Advances*, 6, eaba6790, <https://doi.org/10.1126/sciadv.aba6790>, 2020.

- 822 Leine, R. I., Schweizer, A., Christen, M., Glover, J., Bartelt, P., and Gerber, W.: Simulation of rockfall trajectories with
823 consideration of rock shape, *Multibody Syst Dyn*, 32, 241–271, <https://doi.org/10.1007/s11044-013-9393-4>, 2014.
- 824 Leith, K., Moore, J. R., Amann, F., and Loew, S.: In situ stress control on microcrack generation and macroscopic extensional
825 fracture in exhuming bedrock: FRACTURE GENERATION IN EXHUMING BEDROCK, *Journal of Geophysical Research:*
826 *Solid Earth*, 119, 594–615, <https://doi.org/10.1002/2012JB009801>, 2014.
- 827 Loye, A., Jaboyedoff, M., and Pedrazzini, A.: Identification of potential rockfall source areas at a regional scale using a DEM-
828 based geomorphometric analysis, *Nat. Hazards Earth Syst. Sci.*, 9, 1643–1653, <https://doi.org/10.5194/nhess-9-1643-2009>,
829 2009.
- 830 Lu, G., Caviezel, A., Christen, M., Demmel, S. E., Ringenbach, A., Bühler, Y., Dinneen, C. E., Gerber, W., and Bartelt, P.:
831 Modelling rockfall impact with scarring in compactable soils, *Landslides*, 16, 2353–2367, <https://doi.org/10.1007/s10346-019-01238-z>, 2019.
- 833 Lu, G., Ringenbach, A., Caviezel, A., Sanchez, M., Christen, M., and Bartelt, P.: Mitigation effects of trees on rockfall hazards:
834 does rock shape matter?, *Landslides*, 18, 59–77, <https://doi.org/10.1007/s10346-020-01418-2>, 2021.
- 835 Luckman, B. H.: Rockfalls and rockfall inventory data: Some observations from surprise valley, Jasper National Park, Canada,
836 *Earth Surface Processes*, 1, 287–298, <https://doi.org/10.1002/esp.3290010309>, 1976.
- 837 Macpherson, A. E., Nicolsky, D. J., and Suleimani, E. N.: Digital elevation models of Skagway and Haines, Alaska:
838 Procedures, data sources, and quality assessment, *Alaska Division of Geological & Geophysical Surveys*,
839 <https://doi.org/10.14509/29143>, 2014.
- 840 Marquínez, J., Menéndez Duarte, R., Farias, P., and Jiménez Sánchez, M.: Predictive GIS-Based Model of Rockfall Activity
841 in Mountain Cliffs, *Natural Hazards*, 30, 341–360, <https://doi.org/10.1023/B:NHAZ.0000007170.21649.e1>, 2003.
- 842 Matasci, B., Stock, G. M., Jaboyedoff, M., Carrea, D., Collins, B. D., Guérin, A., Matasci, G., and Raveland, L.: Assessing
843 rockfall susceptibility in steep and overhanging slopes using three-dimensional analysis of failure mechanisms, *Landslides*,
844 15, 859–878, <https://doi.org/10.1007/s10346-017-0911-y>, 2018.
- 845 Matsuoka, N. and Sakai, H.: Rockfall activity from an alpine cliff during thawing periods, *Geomorphology*, 28, 309–328,
846 [https://doi.org/10.1016/S0169-555X\(98\)00116-0](https://doi.org/10.1016/S0169-555X(98)00116-0), 1999.
- 847 Mayer, T., Deprez, M., Schröer, L., Cnudde, V., and Draebing, D.: Quantifying frost-weathering-induced damage in alpine
848 rocks, *The Cryosphere*, 18, 2847–2864, <https://doi.org/10.5194/tc-18-2847-2024>, 2024.
- 849 Meentemeyer, R. K. and Moody, A.: Automated mapping of conformity between topographic and geological surfaces,
850 *Computers & Geosciences*, 26, 815–829, [https://doi.org/10.1016/S0098-3004\(00\)00011-X](https://doi.org/10.1016/S0098-3004(00)00011-X), 2000.
- 851 Menounos, B., Goehring, B. M., Osborn, G., Margold, M., Ward, B., Bond, J., Clarke, G. K. C., Clague, J. J., Lakeman, T.,
852 Koch, J., Caffee, M. W., Gosse, J., Stroeven, A. P., Seguinot, J., and Heyman, J.: Cordilleran Ice Sheet mass loss preceded
853 climate reversals near the Pleistocene Termination, *Science*, 358, 781–784, <https://doi.org/10.1126/science.aan3001>, 2017.
- 854 Messenzehl, K., Meyer, H., Otto, J.-C., Hoffmann, T., and Dikau, R.: Regional-scale controls on the spatial activity of rockfalls
855 (Turtmann Valley, Swiss Alps) — A multivariate modeling approach, *Geomorphology*, 287, 29–45,
856 <https://doi.org/10.1016/j.geomorph.2016.01.008>, 2017.

- 857 Michoud, C., Derron, M.-H., Horton, P., Jaboyedoff, M., Baillifard, F.-J., Loye, A., Nicolet, P., Pedrazzini, A., and Queyrel,
858 A.: Rockfall hazard and risk assessments along roads at a regional scale: example in Swiss Alps, *Natural Hazards and Earth
859 System Sciences*, 12, 615–629, <https://doi.org/10.5194/nhess-12-615-2012>, 2012.
- 860 Moore, J. R., Sanders, J. W., Dietrich, W. E., and Glaser, S. D.: Influence of rock mass strength on the erosion rate of alpine
861 cliffs, *Earth Surface Processes and Landforms*, 34, 1339–1352, <https://doi.org/10.1002/esp.1821>, 2009.
- 862 Moos, C., Khelidj, N., Guisan, A., Lischke, H., and Randin, C. F.: A quantitative assessment of rockfall influence on forest
863 structure in the Swiss Alps, *Eur J Forest Res*, 140, 91–104, <https://doi.org/10.1007/s10342-020-01317-0>, 2021.
- 864 Munson, M.: Railroad Dock landslides continue, declaration of emergency in place, *The Skagway News*, 12th August, 2022a.
- 865 Munson, M.: Rockslide at cruise ship dock – Skagway’s Railroad Dock has limited use, *The Skagway News*, 23rd June, 2022b.
- 866 Nash, D., Rutz, J. J., and Jacobs, A.: Atmospheric Rivers in Southeast Alaska: Meteorological Conditions Associated With
867 Extreme Precipitation, *Journal of Geophysical Research: Atmospheres*, 129, e2023JD039294,
868 <https://doi.org/10.1029/2023JD039294>, 2024.
- 869 Oliinyk, M., Bubniak, I., and Vikhot, Y.: Using Move software by geological field works, *International Conference of Young
870 Professionals «GeoTerrace-2020»*, 1–5, <https://doi.org/10.3997/2214-4609.20205706>, 2020.
- 871 Paranunzio, R., Laio, F., Nigrelli, G., and Chiarle, M.: A method to reveal climatic variables triggering slope failures at high
872 elevation, *Nat Hazards*, 76, 1039–1061, <https://doi.org/10.1007/s11069-014-1532-6>, 2015.
- 873 Paranunzio, R., Laio, F., Chiarle, M., Nigrelli, G., and Guzzetti, F.: Climate anomalies associated with the occurrence of
874 rockfalls at high-elevation in the Italian Alps, *Natural Hazards and Earth System Sciences*, 16, 2085–2106,
875 <https://doi.org/10.5194/nhess-16-2085-2016>, 2016.
- 876 Pawlik, Ł., Phillips, J. D., and Šamonil, P.: Roots, rock, and regolith: Biomechanical and biochemical weathering by trees and
877 its impact on hillslopes—A critical literature review, *Earth-Science Reviews*, 159, 142–159,
878 <https://doi.org/10.1016/j.earscirev.2016.06.002>, 2016.
- 879 Poage, N. J., Marshall, D. D., and McClellan, M. H.: Maximum Stand-Density Index of 40 Western Hemlock–Sitka Spruce
880 Stands in Southeast Alaska, *Western Journal of Applied Forestry*, 22, 99–104, <https://doi.org/10.1093/wjaf/22.2.99>, 2007.
- 881 Priest, S. D. and Hudson, J. A.: Estimation of discontinuity spacing and trace length using scanline surveys, *International
882 Journal of Rock Mechanics and Mining Sciences & Geomechanics Abstracts*, 18, 183–197, [https://doi.org/10.1016/0148-
9062\(81\)90973-6](https://doi.org/10.1016/0148-
883 9062(81)90973-6), 1981.
- 884 Rapp, A.: Talus slopes and mountain walls at Tempelfjorden, Spitsbergen : a geomorphological study of the denudation of
885 slopes in an Arctic locality, *Skritfter, Norsk Polarinstitut*, 119, 1960.
- 886 Ravanel, L., Deline, P., Lambiel, C., and Vincent, C.: Instability of a High Alpine Rock Ridge: the Lower Arête Des
887 Cosmiques, Mont Blanc Massif, France, *Geografiska Annaler: Series A, Physical Geography*, 95, 51–66,
888 <https://doi.org/10.1111/geoa.12000>, 2013.
- 889 Rempel, A. W., Marshall, J. A., and Roering, J. J.: Modeling relative frost weathering rates at geomorphic scales, *Earth and
890 Planetary Science Letters*, 453, 87–95, <https://doi.org/10.1016/j.epsl.2016.08.019>, 2016.

- 891 Ringenbach, A., Bebi, P., Bartelt, P., Rigling, A., Christen, M., Bühler, Y., Stoffel, A., and Caviezel, A.: Shape still matters:
892 rockfall interactions with trees and deadwood in a mountain forest uncover a new facet of rock shape dependency, *Earth*
893 *Surface Dynamics*, 11, 779–801, <https://doi.org/10.5194/esurf-11-779-2023>, 2023.
- 894 Roering, J. J., Dedinsky, K., Grilliot, M., Wachino, I. D., and Cash, R.: Skagway Landslide Hazard, RAPID Facility,
895 <https://doi.org/doi.org/10.17603/ds2-2e3p-yn12>, 2025.
- 896 Rosser, N. and Massey, C.: Rockfall hazard and risk, in: *Landslide Hazards, Risks, and Disasters*, Elsevier, 581–622,
897 <https://doi.org/10.1016/B978-0-12-818464-6.00013-5>, 2022.
- 898 Rosser, N., Lim, M., Petley, D., Dunning, S., and Allison, R.: Patterns of precursory rockfall prior to slope failure, *Journal of*
899 *Geophysical Research: Earth Surface*, 112, <https://doi.org/10.1029/2006JF000642>, 2007.
- 900 Royán, M. J., Abellán, A., Jaboyedoff, M., Vilaplana, J. M., and Calvet, J.: Spatio-temporal analysis of rockfall pre-failure
901 deformation using Terrestrial LiDAR, *Landslides*, 11, 697–709, <https://doi.org/10.1007/s10346-013-0442-0>, 2014.
- 902 Ruffner, C. M. and Abrams, M. D.: Relating land-use history and climate to the dendroecology of a 326-year-old *Quercus*
903 *prinus talus* slope forest, *Can. J. For. Res.*, 28, 347–358, <https://doi.org/10.1139/x97-220>, 1998.
- 904 Samodra, G., Chen, G., Sartohadi, J., Hadmoko, D. S., Kasama, K., and Setiawan, M. A.: Rockfall susceptibility zoning based
905 on back analysis of rockfall deposit inventory in Gunung Kelir, Java, *Landslides*, 13, 805–819, <https://doi.org/10.1007/s10346-016-0713-7>, 2016.
- 907 Sarro, R., Rossi, M., Reichenbach, P., and Mateos, R. M.: From rockfall source areas identification to susceptibility zonation:
908 a proposed workflow tested in El Hierro (Canary Islands, Spain), *Natural Hazards and Earth System Sciences Discussions*, 1–
909 30, <https://doi.org/10.5194/nhess-2024-85>, 2024.
- 910 Scheidl, C., Heiser, M., Vospernik, S., Lauss, E., Perzl, F., Kofler, A., Kleemayr, K., Bettella, F., Lingua, E., Garbarino, M.,
911 Skudnik, M., Trappmann, D., and Berger, F.: Assessing the protective role of alpine forests against rockfall at regional scale,
912 *Eur J Forest Res*, 139, 969–980, <https://doi.org/10.1007/s10342-020-01299-z>, 2020.
- 913 Statham, I.: A scree slope rockfall model, *Earth Surface Processes*, 1, 43–62, <https://doi.org/10.1002/esp.3290010106>, 1976.
- 914 van Steijn, H.: Long-term landform evolution: evidence from talus studies, *Earth Surface Processes and Landforms*, 27, 1189–
915 1199, <https://doi.org/10.1002/esp.420>, 2002.
- 916 Stock, G. M. and Collins, B. D.: Quantitative Rockfall hazard and risk assessment for Yosemite Valley, Yosemite National
917 Park, California, USGS Scientific Investigations Report 2014-5129, 2014.
- 918 Stock, G. M., Bawden, G. W., Green, J. K., Hanson, E., Downing, G., Collins, B. D., Bond, S., and Leslar, M.: High-resolution
919 three-dimensional imaging and analysis of rock falls in Yosemite Valley, California, *Geosphere*, 7, 573–581,
920 <https://doi.org/10.1130/GES00617.1>, 2011.
- 921 Stoffel, M., Lièvre, I., and Monbaron, M.: Seasonal timing of rockfall activity on a forested slope at Täschgufer (Swiss Alps)
922 - a dendrochronological approach, *Zeitschrift für Geomorphologie*, 89–106, 2005.
- 923 Stoffel, M., Trappmann, D. G., Coullie, M. I., Ballesteros Cánovas, J. A., and Corona, C.: Rockfall from an increasingly
924 unstable mountain slope driven by climate warming, *Nat. Geosci.*, 1–6, <https://doi.org/10.1038/s41561-024-01390-9>, 2024.

- 925 Terzaghi, R. D.: Sources of Error in Joint Surveys, *Géotechnique*, 15, 287–304, <https://doi.org/10.1680/geot.1965.15.3.287>,
926 1965.
- 927 The Daily Alaskan: SLIDE: Hill again caves in near Moore’s Wharf, *The Daily Alaskan*, 20th October, 1, 1901.
- 928 Thompson, P.: Alaska Department of Transportation & Public Facilities (AKDOT) Geotechnical Asset Management Program,
929 Technical Report STP000S(802)(B), Juneau, AK, 2017.
- 930 Thornton, T. F.: *Our Grandparents’ Names on the Land/Haa Leelk’w Has Aani Saax’u*, University of Washington Press,
931 Seattle, WA, 256 pp., 2010.
- 932 Utlu, M., Öztürk, M. Z., Şimşek, M., and Akgümüş, M. F.: Evaluation of rockfall hazard based on UAV technology and 3D
933 Rockfall Simulations, *International Journal of Environment and Geoinformatics*, 10, 1–16,
934 <https://doi.org/doi.%252010.30897/ijegeo.10323768>, 2023.
- 935 Western Regional Climate Center: <https://wrcc.dri.edu>, last access: 14 August 2025.
- 936 Whalley, B.: Rockfalls, in: *Slope Instability*, Wiley, Chichester, UK, 217–256, 1984.
- 937 Wieczorek, G. F. and Jäger, S.: Triggering mechanisms and depositional rates of postglacial slope-movement processes in the
938 Yosemite Valley, California, *Geomorphology*, 15, 17–31, [https://doi.org/10.1016/0169-555X\(95\)00112-I](https://doi.org/10.1016/0169-555X(95)00112-I), 1996.
- 939 Wright, B. E., Plumb, P., Wright, J., and Biles, F. E.: Historical photographs from U.S. Forest Service research and
940 development activities in Alaska, <https://doi.org/10.2737/RDS-2021-0084>, 2021.
- 941 Wyllie, D. C. and Mah, C. W.: *Rock Slope Engineering*, 4th ed., Spon, 456 pp., 2004.
- 942 Yehle, L. A. and Lemke, R. W.: *Reconnaissance engineering geology of the Skagway area, Alaska with emphasis on evaluation*
943 *of earthquake and other geologic hazards*, USGS Open File Report, 1972.